

1 **Rockwall permafrost dynamics evidenced by Repeated**
2 **and Automated Electrical Resistivity Tomography at**
3 **Aiguille du Midi (3842 m a.s.l., French Alps)**

4
5 Feras Abdulsamad^{1,2}, Josué Bock¹, Florence Magnin¹, Emmanuel Malet¹, André Revil¹,
6 Matan Ben-Asher¹, Jessy Richard^{1,2}, Pierre-Allain Duvillard², Marios Karaoulis³, Thomas
7 Condom⁴, Ludovic Ravanel¹ and Philip Deline¹
8

9 1. EDYTEM, CNRS - Université Savoie Mont-Blanc, 73370 Le Bourget du Lac, France

10 2. Naga Geophysics, 229 rue Joseph Fontanet 73000 Chambéry, France

11 3. School of Geology, Geophysics Department, Aristotle University of Thessaloniki, Thessaloniki, Greece

12 4. Univ. Grenoble Alpes, IRD, CNRS, INRAE, Grenoble-INP, IGE, 38000 Grenoble, France
13

14 **Corresponding author:** Abdulsamad Feras (feras.abdul-samad@univ-smb.fr)

15 **Emails:** feras.abdul-samad@naga-geophysics.com; feras.abdul-samad@univ-smb.fr;
16 andre.revil@univ-smb.fr; ludovic.ravanel@univ-smb.fr; florence.magnin@univ-smb.fr;
17 mkaraoulis@geo.auth.gr; matan.ben-asher@univ-smb.fr; [pierre-allain.duvillard@naga-](mailto:pierre-allain.duvillard@naga-geophysics.com)
18 geophysics.com; josue.bock@laposte.net; emmanuel.malet@univ-savoie.fr;
19 jessy.richard@naga-geophysics.com; thomas.condom@ird.fr; philip.deline@univ-smb.fr

Code de champ modifié

20
21 **Keywords:** Rockwall permafrost dynamics; Active layer thickness; Electrical resistivity
22 tomography; Temperature measurements.
23
24
25

Intended for publication in The Cryosphere

26 **Abstract.** Permafrost degradation significantly affects the stability of rockwalls in high altitude
27 regions. Monitoring rockwall permafrost is essential for assessing potential geohazards. While
28 borehole temperature measurements are the most direct permafrost monitoring approach, they
29 lack often lack of sufficient spatial representation in such highly heterogeneous ground
30 conditions. Conversely, geoelectrical measurements can provide more comprehensive insights
31 into these complex patterns and dynamics. This study investigates the permafrost dynamics and
32 intends to detect potential hydrogeological processes system at the Aiguille du Midi (3842 m
33 a.s.l., French Alps) using repeated and Automated-Electrical Resistivity Tomography (A-ERT)
34 approaches, covering a period of nearly four 3.5 years (06/2020-12/2023). A total of three
35 geoelectrical physical profiles have been installed on three faces of the Aiguille du Midi (N-W,
36 S and E). An automated nomous acquisition system for permanent resistivity monitoring and
37 remote data acquisition is implemented. A time-lapse inversion technique is employed to get
38 the temporal and spatial variations of electrical resistivity at seasonal and interannual time
39 scales. ERT-The data revealed significant variations in active layer thickness across different
40 rock faces, along with a slight decrease in electrical resistivity at depth, indicating permafrost
41 warming over time. However, The ERT results they did not provide clear evidence of water
42 infiltration or pressurization accumulation in rock fractures. Using a petrophysical model,
43 calibrated with laboratory measurements of the temperature dependence of electrical resistivity,
44 we estimated the temperature within the frozen zone from the resistivity measurements (under
45 favorable condition at surface). Validation against direct temperature measurements in a 10-m
46 depth borehole along the NW profile demonstrates an accuracy of approximately ± 1 °C. This
47 research underscores the efficacy of ERT as a promising, non-invasive tool for quantitative
48 monitoring of permafrost dynamics in Alpine environments. It also reveals challenges
49 associated with conducting A-ERT in high mountain rockwall environment, where the contact

50 resistance is very high (~500 k Ω) and sometimes intermittent due to factors such as thunder
51 strikes and rockfalls.

52 1. Introduction

53 Climate change accelerates the degradation of the permafrost in high-mountains areas
54 worldwide (Smith et al., 2022). In the European Alps, permafrost has warmed up to > 1°C at
55 10 m depth, especially in bedrock permafrost (Etzelmüller et al., 2020; Magnin et al., 2024;
56 Noetzi et al., 2024). Over the last decade, there has been a continuous increase in rockfall
57 events, particularly those impacting permafrost in the European Alps (Cathala et al., 2024;
58 Jacquemart et al., 2024; Ravel et al., 2017). Infrastructures located in high altitude are
59 increasingly affected by these events (Duvillard et al., 2021, 2018; Hartmeyer et al. 2020).
60 Permafrost degradation/warming of the rock mass can also locally be accelerated by heat
61 advection through water infiltration in fractures(see for example Hasler et al., (2011) for a
62 laboratory experiment; Magnin and Josnin (2021) for a numerical experiment), leading
63 to/causing erosion of the ice-infill (Hauck and Hilbich, 2024; Hartmeyer et al. 2020). As a result,
64 a loss of bonding between rock and ice may occur, which in turn alters the mechanical properties
65 of such assemblage (Mamot et al., 2018; Krautblatter et al., 2013). Therefore, understanding
66 the thermo-hydrogeological dynamics of steep Alpine rock faces is essential for assessing
67 potential geohazards associated with permafrost degradation.

68 To assess permafrost warming, one approach is to directly determine and monitor
69 rockwall temperatures using temperature sensors installed at the rock surface or in boreholes
70 (e.g., Magnin et al., 2024). Although borehole temperature monitoring is still the only direct
71 method to detect ~~and monitor the occurrence of~~ permafrost, it provides only point-scale
72 information, while its distribution and evolution can be highly variable in extreme
73 topographical conditions. In addition, boreholes in rockwall at high altitude are logistically
74 difficult to realize. ~~and They~~ are also expensive and invasive.

75 On the other sidehand, geophysical measurements provide higher spatial coverage with
76 respect to boreholes. Various non- or minimally intrusive methods have been applied to
77 evaluate permafrost, including Refraction Seismic Tomography (RST) (*e.g.*, Steiner et al.,
78 2019; Draebing 2016), Ground Penetrating Radar (GPR) (Campbell et al., 2018), Electrical
79 Resistivity Tomography (ERT) (*e.g.*, Mollaret et al., 2020; Krautblatter and Hauck 2007) and
80 Induced Polarization (IP) (Maierhofer et al., 2024; Abdulsamad et al., 2019; Duvillard et al.,
81 2018; Doetsch et al., 2015). Combined geophysical methods can take advantage of the
82 complementary petrophysical and spatial sensitivities of these different methods. For instance,
83 ERT measurement was combined with RST to evaluate ice, air, water, and rock contents
84 (Mewes et al., 2017; Hauck et al., 2011). Recently, joint inversion of ERT and RST could
85 reduce the uncertainties in the evaluation of air, water, ice and rock contents (Pavoni et al.,
86 2023; Steiner et al., 2021; Mollaret et al., 2020; Wagner et al., 2019). IP measurements
87 (providing tomograms of the electrical conductivity and normalized chargeability) have been
88 recently used to assess the distribution of permafrost temperature, relying on laboratory
89 calibration and a petrophysical (physics-based) model connecting resistivity and normalized
90 chargeability with temperature under frozen and unfrozen conditions (see Moser et al., 2025;
91 Duvillard et al., 2021, 2018, and references therein).

92 In the last two decades, ERT has become an increasingly popular tool in permafrost
93 studies (*e.g.*, Herring et al., 2023; Farzamain et al., 2020; Magnin et al., 2015a; Krautblatter et
94 al., 2010). Herring et al. (2023) provides a review of the use of ERT method in permafrost
95 research, detailing both the advantages and limitations of this method in such a context. A
96 significant advantage of using electrical resistivity measurements to assess mountain
97 permafrost is that the freezing and thawing of water filling pores are associated with
98 considerable changes in resistivity (generally between one to three orders of magnitude, see

99 Coperey et al., 2019). Because of this sensitivity, electrical resistivity tomograms can be used
100 to assess the presence and distribution of permafrost.

101 Repeated ERT measurements at specific time intervals using the same survey geometry
102 can be used to track the temporal and spatial evolution of permafrost over time (*e.g.*, Offer et
103 al., 2025, Hilbich et al., 2008). However, rapid changes due to water flow, infiltration or
104 drainage (such as during snowmelt or rainfall) may not be captured by monthly or seasonally
105 repeated measurements (Krautblatter et al., 2010). Alternatively, continuous resistivity
106 measurements, known as Automated-ERT (A-ERT) or ERT monitoring, offer the ability to
107 track the ongoing evolution of permafrost and capture rapid, heterogeneous and non-linear
108 changes in its temperature and ice content (*e.g.*, Scandroglio et al., 2021; Doetsch et al., 2015).
109 A-ERT over period of several years has been recently used to track the degradation of
110 permafrost associated with global warming (Mollaret et al., 2019; Keusching et al., 2017;
111 Doetsch et al., 2015; Hilbich et al., 2008).

112 Furthermore, the time-lapse inversion of geophysical data derived from [a](#) fixed
113 monitoring network provides a succession of tomograms showing the spatial and temporal
114 changes in subsurface resistivity (see; Karaoulis et al., 2013; Loke, 1999). The results of time-
115 lapse inversions of apparent resistivity data can be directly linked to the evolution of permafrost
116 throughout the annual cycle or to rapid variations caused by water infiltration or drainage during
117 short periods of time ([Cimpoiasu et al., 2025](#); Keusching et al., 2017; Hilbich et al., 2008).

118 That said, A-ERT at high altitudes (>3500 m) and over a multi-profile setting has not
119 yet been tested for pluriannual permafrost monitoring. The use of A-ERT under high-altitude
120 conditions presents specific challenges due to extreme topographical and climatic conditions as
121 well as meteorological events. However, it could provide valuable information about the
122 hydrogeological system and the evolution of permafrost in environments where its distribution
123 and dynamic are highly heterogeneous.

124 In this study, we present the results of an A-ERT survey conducted over nearly four
 125 years (2020-2023) at Aiguille du Midi (AdM) in the Mont-Blanc massif (French Alps). The site
 126 consists of massive and fractured granite and includes infrastructures such as tunnels and
 127 elevators. Water infiltration was observed at various locations within the tunnels. The objective
 128 of this study is to investigate permafrost dynamics from infra-seasonal to multiyear timescales
 129 and through various rock faces of ~~a~~the same site. Our goals ~~include~~are: (1) evaluating the
 130 potential of A-ERT to characterize seasonal to pluriannual permafrost dynamics, its
 131 heterogeneity and non-linearity in steep alpine rockwalls; (2) assessing the accuracy of
 132 temperature derived from resistivity measurements; and (3) attempting to detect potential water
 133 circulation pathways ~~studying the hydrogeological system, including water infiltration and~~
 134 ~~drainage~~ in fractures, along with their thermal impacts. For this objective, a total of three ERT
 135 profiles were deployed downwards from the summit in three directions: North-West (NW),
 136 South (S) and East (E). Each profile consists of 32 electrodes spaced at 5 m. In addition to field
 137 data, laboratory resistivity measurements were conducted on granite core samples, in both
 138 unfrozen and frozen conditions. Furthermore, temperature ~~which~~ was continuously monitored
 139 in a 10 m-deep borehole along the NW profile and was~~is~~ used to quantitatively evaluate the
 140 accuracy of temperature estimates ~~ion derived from~~using geophysical measurements of
 141 electrical resistivity.

142 2. Study site

143 We investigate the Aiguille du Midi (3842 m a.s.l.), which is the highest and most
 144 western summit of the Aiguilles de Chamonix (Fig. 1a). It is located on the NW flank of the
 145 Mont-Blanc massif. It includes three peaks that are all connected by human-made bridges and
 146 galleries and hosts major touristic and technical infrastructures. During the summer season,
 147 AdM is visited by approximately 5000 visitors per day, who are transported from the city of
 148 Chamonix by cable car, making it one of the most intensively frequented high-alpine sites in

a mis en forme : Police :Non Gras, Police de script complexe
 :Non Gras

149 ~~the European Alps. In average, AdM is visited in summer by around 5000 visitors a day~~
150 ~~transported from the city of Chamonix by cable cars. The appearance of the summit of AdM~~
151 ~~has been greatly affected by the construction and developments carried out since the 1950s (see~~
152 ~~Fig. 4). Since the 1950s, the morphology and appearance of the summit have been strongly~~
153 ~~modified by construction and infrastructure development (Fig. 1). These factors, combined with~~
154 ~~the extreme topography characterized by near-vertical rock walls with an average slope of 78°~~
155 ~~on the northwestern face, make the site particularly prone to rock instability processes.~~
156 ~~Consequently, AdM represents a critical location where geotechnical and geophysical~~
157 ~~monitoring is essential to ensure the long-term stability of the infrastructures and the safety of~~
158 ~~visitors.~~ Our study focuses on the central peak, which is the highest among the three, and which
159 hosts the cable-car station connecting AdM to Pointe Helbronner with the *Panoramic Mont-*
160 *Blanc* cable car. ~~The topography is characterized by vertical rock walls with an average slope~~
161 ~~of 78° on the North-West face.~~

162 The lithology in the study area is dominated by massive granite with a very low porosity
163 (~ 0.01, Magnin et al., 2015a). The highest parts (3740 to 3840 m a.s.l.) of the peak tend to be
164 steep, contain few large fractures, and, in places, are characterized by vertical foliation bands
165 and small cracks (Magnin et al., 2015b). Figure 2 shows the mean monthly and annual air
166 temperature at AdM during the study period. The year 2021 was the coolest year (yearly
167 averages: -5.8 °C, -6.9 °C, -5.3 °C, and -5.7 °C from 2020 to 2023, respectively), and 2022 the
168 warmest especially due to extremely warm summer that had important consequences on rock
169 temperature (Magnin et al., 2024; Bruel et al., 2026).

170 In order to evaluate the thermal state and the distribution of permafrost at AdM, three
171 boreholes have been drilled in 2009. They are labeled BH-NW on the NW face, BH-S on the
172 South face and BH-E on the East face. Each borehole is 10-m-deep and 66 mm in diameter and
173 was drilled normal to the topography (their position is shown in Fig. 1b-d). Each borehole is

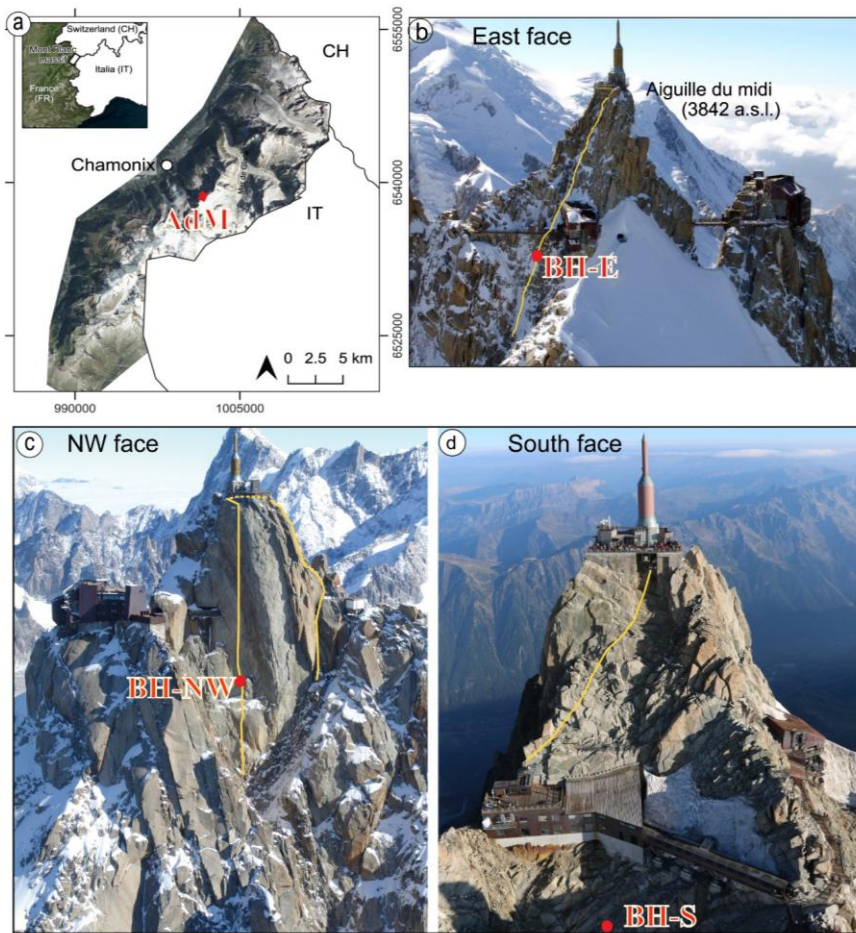
174 equipped with 15-thermistor strings calibrated in an ice-water bath and then placed at different
175 depths in the borehole. Figure A1 shows the temperature measured in BH-NW and BH-S at
176 different dates.

177 The temperature of the permafrost core shows significant variability between the South
178 and North-West faces of the AdM~~from one face to another~~. For example, at a depth of 10
179 meters, the temperature is approximately -4 °C on the NW face, while it is around -1 °C on the
180 sun-exposed S face (Magnin et al., 2024). These temperature differences indicate the presence
181 of strong temperature gradients within the rock mass. In the same way, the Active Layer
182 Thickness (ALT, *i.e.*, the maximum seasonal thaw layer) is also highly variable as interpolated
183 between temperature sensors: it is observed to be around 1.3 to 2.7 m in summer on the NW
184 side, while it reaches 4.8 to 7.6 m on the S side in the early fall. Below this depth, permafrost
185 is present (Magnin et al., 2024). Figure A1 (appendix A) shows the temperature variation over
186 depth in boreholes BH-NW and BH-S on different dates

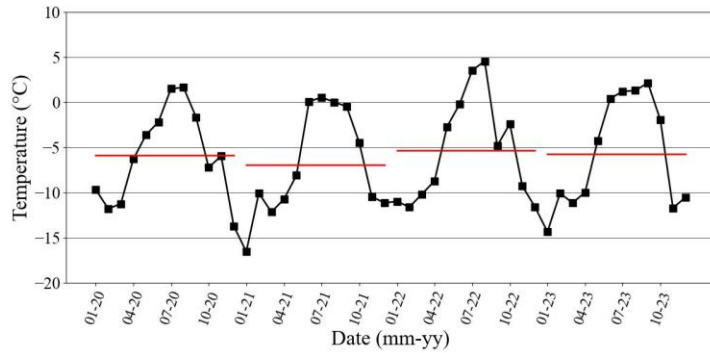
187 BH-NW is located along an electrical resistivity profile (NW profile) and is positioned
188 between electrodes 8 and 9 (counted from the bottom) of the NW profile (see Fig. 1c). The
189 temperature measured in this borehole is used to assess the accuracy of the temperature derived
190 from ERT results using the petrophysical model presented in the next section.

191

192



193
 194 **Figure 1.** Study site location and geophysical survey setting. The yellow lines indicate the approximate
 195 positions of electrical resistivity profiles on each side (NW, E and S profiles). The red dots denote the
 196 borehole locations. (a) Location of the study site (Aiguille du Midi (AdM)), in the Mont Blanc massif
 197 (here, the French side). The electrical resistivity profile and borehole locations at the East face(b), at
 198 the North-West face (c) and at the South face (d).
 199



200

201 **Figure 2.** Monthly average air temperature (°C) at AdM during the survey period (Data from the
 202 meteorological station of Institute of Environmental Geosciences at the Aiguille du Midi). Horizontal
 203 bars show the annual average air temperature.

204

205 3. Electrical conductivity - temperature relationship

206 The electrical conductivity of a rock represents its ability to conduct an electrical current
 207 under the application of an imposed electrical field. The electrical conductivity (inverse of the
 208 electrical resistivity) of a rock depends on its porosity ϕ (dimensionless), water content θ
 209 (dimensionless), pore water conductivity, Cation Exchange Capacity (CEC), and rock
 210 temperature T (in °C) (e.g., Revil et al., 1998).

211 Above the freezing point (typically, but not necessary, around 0°C), electrical
 212 conductivity ($\sigma(T)$ in S m^{-1}) increases linearly with temperature according to Revil et al. (1998):

$$213 \quad \sigma(T) = \sigma(T_0)[1 + \alpha_T(T - T_0)], \quad (1)$$

214 where $\alpha_T = 0.021 \pm 0.02 \text{ } ^\circ\text{C}^{-1}$, $T_0 = 25^\circ\text{C}$ denotes the reference temperature, and $\sigma(T_0)$ denotes
 215 the conductivity of the rock at the reference temperature. Equation (1) results from the effect of
 216 temperature on the mobility of the ions in the pore water and in the electrical double layer
 217 coating the surface of the grains.

218

219 In contrast, under freezing conditions, temperature variations have a significant
 220 influence on electrical conductivity because of the occurrence of an insulating phase (*i.e.*, ice
 221 formation) in the pore space and despite the increase in the salinity of the pore water with
 222 temperature decrease. This temperature dependence of electrical conductivity can be modeled
 223 as follows (see details in Duvillard et al., 2018; 2021; Coperey et al., 2019):

$$224 \quad \sigma(T) \approx \left[(\phi - \theta_r) \exp\left(-\frac{T - T_F}{T_C}\right) + \theta_r \right] \frac{\sigma(T_0)}{\phi} [1 + \alpha_T(T - T_0)], \quad (2)$$

225 where θ_r (dimensionless) denotes the residual water content when $T \ll T_F$, T_F denotes the
 226 liquidus or freezing point/temperature, T_C denotes a characteristic temperature controlling the
 227 transition between the unfrozen state and the frozen state, and $\phi - \theta_r$ denotes the maximum
 228 volumetric ice content at low temperatures. Equation (2) provides the opportunity to convert
 229 electrical conductivity or electrical resistivity tomogram measured in the field to a temperature
 230 distribution (*e.g.*, Duvillard et al., 2021).

231

232 4. Methods

233 4.1 Laboratory measurements

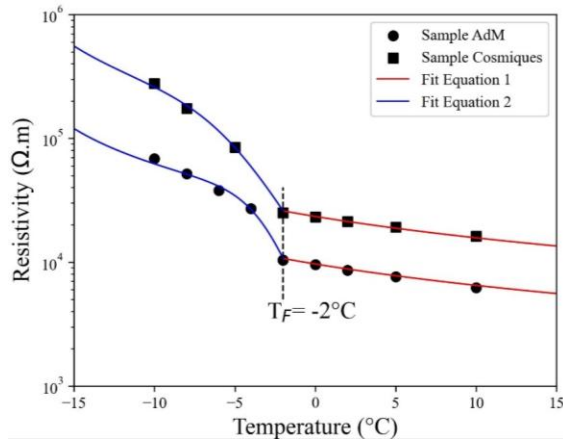
234 In order to calibrate our field measurements and evaluate the parameters (*e.g.*, T_C , θ_r)
 235 in the petrophysical model discussed above (Section 3), we conducted an electrical conductivity
 236 experiment on a granite rock sample collected from an outcrop ~~at~~ the study site. The cube-
 237 shaped granite sample (dimensions: $5 \times 5 \times 5 \text{ cm}^3$) was dried during 24 h at approximately 100
 238 °C, then saturated under vacuum with degassed water. The saturated water conductivity was
 239 conductivity was measured to be 0.016 S m^{-1} at equilibrium at $T = 25^\circ\text{C}$. This value is
 240 representative of the conductivity of infiltrating water collected and measured in galleries at
 241 the AdM site (approximately $150 \mu\text{S/cm}$ or 0.015 S m^{-1} , see Ben-Asher et al. (2026). water from
 242 the field (about $150 \mu\text{S/cm}$ or 0.015 S m^{-1}) at equilibrium at $T = 25^\circ\text{C}$. The sample was left in

243 the solution for several weeks to reach chemical equilibrium before performing the laboratory
244 measurements. The ~~Sample-sample~~ was characterized by a very low measured porosity $\phi =$
245 0.014.

246 For thermal-resistivity analysis, the sample was placed in a heat-resistant insulating bag
247 immersed in a thermostat bath (KISS K6 from Huber; dimensions: 210×400×546 mm³; bath
248 volume: 4.5 L). The temperature of the bath was controlled with a precision of 0.1 °C. Glycol
249 was used as the heat carrying fluid (Coperey et al., 2019). Thin Carbon film electrodes were
250 used for both current injections and potential measurement. The complex conductivity spectra
251 were obtained over the temperature range of +10 to -10 °C, using a high-precision impedance-
252 meter ZEL-SIP04-V02 (Zimmermann et al., 2008). The resistivity measurements reported here
253 are at a frequency of 1 Hz (Coperey et al., 2019).

254 Figure 3 presents the measurement results for the granite sample from the study site
255 (labeled Sample AdM), alongside measurements of another granite sample (Sample
256 Cosmiques) collected from a nearby site at the lower Cosmiques Ridge (Mont-Blanc massif,
257 3613 m a.s.l.), as reported by Duvillard et al. (2021). The experimental datasets are presented
258 along with data fits, using Equations 1 for temperatures above the freezing point, and Equation
259 2 for temperatures below the freezing point. T-We see that the model proposed in Section 3
260 successfully fits is able to fit the data above and below the freezing temperature, providing a
261 proxy for connecting electrical conductivity ~~or electrical resistivity~~ to temperature.

262



263

264 **Figure 3.** Resistivity-temperature relationship from laboratory measurements on two granite samples
 265 from (1) the study site (Sample AdM), and (2) from the Cosmiques ridge, Mont-Blanc massif, West
 266 (3613 m a.s.l.) (Sample labeled Cosmiques). T_F denotes the freezing temperature. The solid lines
 267 correspond to the fits using the Equation 1 (red lines) and Equation 2 (blue lines), in unfrozen and frozen
 268 conditions, respectively. The parameters of the model in Equation 2 are ($T_c = -1.3$ °C, $\theta_r = 0.004$, $\sigma(T_0) =$
 269 2.3×10^{-4} S m⁻¹) for Sample AdM, and ($T_c = -2.17$ °C, $\theta_r = 0.004$, $\sigma(T_0) = 9.5 \times 10^{-5}$ S m⁻¹) for Sample
 270 Cosmiques.

271

272 4.2 ERT Data acquisition

273 ERT has been conducted over a four-years period (06/2020 - 12/2023). A total of three
 274 cables, each with 32 take-outs spaced 5 m (for a profile length of 155 m), were installed. The
 275 three cables were deployed downwards from the summit in three directions: North-West (NW),
 276 East (E) and South (S). The S profile starts at the South side and passes to the North-West side
 277 around mid-distance (see Fig. 1c, d). The cables installation was gradually (over a year) starting
 278 from NW side (installed in June 2020), then on the South side (installed in July and August
 279 2020), and finally on the East side (installation finished in March 2021 because of snowpack in
 280 2020 at this side). In order to ensure good electrical contact between electrodes and rock mass,
 281 stainless steel (A4/316) climbing bolts (Fischer 10×126 mm) poured in salty bentonite were
 282 used and placed firmly in holes drilled in the rock. A specially designed jumper was used to

283 attach each take-out to the bolt to ensure maximum contact. The resistivity cables were attached
284 to anchors to minimize damage from rockfall and snow pressure.

285 A LS2-Terrameter (ABEM) with internal impedance of 20 M Ω was used for the data
286 acquisition. The ERT device and control system for monitoring were deployed inside the
287 summit station with network access, power connection, and overvoltage protection. Data
288 acquisition was fully automated and remotely controlled since September 2021. Finally, the
289 position of every electrode was measured using a differential GPS when the signal is available
290 and a theodolite in steep areas. The measurements were carried out using a Wenner
291 configuration, which provides a high signal-to-noise ratio and is widely used in mountain
292 permafrost environments (Mollaret et al., 2020; Krautblatter and Hauck, 2007; Dahlin and
293 Zhou, 2004). Each profile consists of 155 data points. An injected current ranging from 0.1 mA
294 to 200 mA was applied, with a maximum stack number of 4 was applied to ensure a standard
295 deviation of less than 5 % in the measured resistivity. The first measurements were performed
296 in June 2020. Between June 2020 and September 2021, ERT measurements were repeated
297 occasionally. Then the continuous measurements started in late September 2021 after
298 developing an automated system of acquisition. Datasets were daily recorded for each profile
299 (NW, S and E profiles).

300 A Contact Resistance (CR) test was performed before each series of measurements. A
301 high contact resistance in the rock wall (>100 k Ω) was encountered throughout the entire survey
302 period, which posed a challenge to the quality and continuity of data acquisition. CR varies
303 between a few k Ω and 10 000 k Ω . However, beyond a CR threshold, the ERT measurements
304 lose their accuracy. Electrodes with high CR (>600 k Ω) are excluded automatically by the LS2,
305 leading to gaps in the pseudo-section of apparent resistivity. Special efforts were made to reduce
306 CR and improve the electrode/rock contact, including the addition of salty water, using copper
307 electrodes and duplicate ~~electrode~~electrodes. The latter one resulted in a significant and a

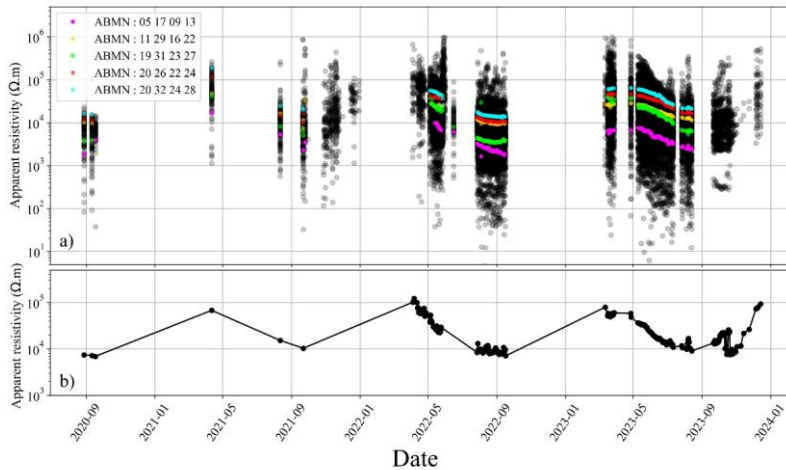
308 ~~durable~~ durable improvement in ~~RCR~~ (one order of magnitude reduction in CR). Figure B1
 309 shows the temporal evolution of CR at profiles S and NW, ~~as well as and the~~ gaps in the A-
 310 ERT measurements caused by cable defects. The periods highlighted by dotted lines correspond
 311 to time intervals during which comparison of CR before and after electrode doubling can be
 312 made.

313 The A-ERT ran into numerous software and hardware issues, resulting in unsystematic
 314 data gaps. The E face cable was severely damaged by a lightning strike, before being totally
 315 destroyed by an uncontrolled rock purge. Additionally, NW and S cables were both damaged
 316 by rockfalls, leading to significant data gaps (see Fig. 4 and Fig. B1). Repairing or replacing
 317 the damaged cables was not possible for several reasons (e.g., limited access to the cable path
 318 because of accumulated snowpack), Data acquisition on the Eastern side (E profile)
 319 encountered numerous challenges related to contact resistance, rockfalls and cable connections,
 320 resulting in long gaps and insufficient data for long time analysis or time-lapse inversion.

322 4.3. Data processing and inversion

323 The apparent resistivities were calculated using the open-source package pyGIMLi
 324 (Rücker et al., 2017), which combines measured resistances and electrode positions. Figure 4
 325 shows the temporal distribution of the measured apparent resistivities ~~measured~~ and the
 326 averaged apparent resistivity along the S-profile, with examples of time series ~~(shown in~~
 327 ~~different colors)~~ of measured apparent resistivities obtained using various quadrupole
 328 configurations (~~ABMNB~~, shown in different colors). The majority of measured apparent
 329 resistivities are distributed over three ~~orders of magnitude decades~~ (100 Ω .m to 100 k Ω .m), with
 330 few data points out of this range.

a mis en forme : Non Surlignage



331
 332 **Figure 4.** Distribution of measured apparent resistivity. a)- daily distribution of the apparent resistivity
 333 over time at the S face (approximately 300 datasets). Colored lines present examples of resistivity times
 334 series, each corresponding to a different set of quadrupoles (AMNB). b) Mean daily measured apparent
 335 resistivity at the S face.

336
 337 For datasets used in inversion, a systematic quality-control procedure was applied prior
 338 to processing the selected data were subjected to the following analysis. The primary selection
 339 criterion was the number of connected electrodes within each pseudo-section. We tolerated
 340 up to four unconnected electrodes (typically due to high contact resistance because of high RC)
 341 were tolerated, in a pseudo-section depending on their positions, since as the electrode
 342 contributions of electrodes is are not equal in the pseudo-section. After selecting valid datasets,
 343 outliers removal was performed. To define appropriate filtering threshold, within each pseudo-
 344 section were removed. For data filtering, we analyzed individually analyzed few representative
 345 pseudo-sections acquired (at different times (in autumn summer and; spring (completed
 346 datasets)), As a result of this analysis we decided to apply filtered outliers out of the range
 347 (300 Ω m - 20 k Ω m) for data measured in summer and autumn, and out of range (300 Ω m - 200
 348 k Ω m) for data measured in spring and winter. More data filtered at higher resistivities, where
 349 data quality is usually poor. Table C1 (appendix C) summarizes the data presented in this study.

350 ~~In most cases, Most datasets have~~ more than 80 % of the originally recorded data points were
351 retained in each pseudo-section after filtering.

352 The inversion of the electrical resistivity datasets was performed using the open-source
353 package pyGIMLi (Rücker et al., 2017; Günther et al., 2006). The inversion uses a Gauss-
354 Newton minimization algorithm of a cost-function penalizing the roughness of the electrical
355 resistivity distribution on an irregular grid (Günther et al., 2006). In the absence of a reciprocal
356 dataset to estimate errors in measurements, we used a linear error model which assumed 5 %
357 relative error and absolute error $1e5$. The parameters used in the inversion process are $zWeight$
358 = 10 and smoothness (λ) equal one~~=1~~. The inversion parameters $zWeight$ is~~was~~ chosen
359 higher than one~~1~~ to enhance the vertical discontinuities and vertical structures (*i.e.*, the active
360 layer, infrastructures), during the inversion process. Then, an iterative process was conducted
361 to select the smoothness parameter (λ) that minimizes the data misfit of individual
362 inversions of a reference dataset (data of 30/06/2020). In order to track the seasonal and
363 interannual variations in the permafrost, a time-lapse inversion approach was employed. In this
364 case, the reference model was moved along with the inversion so that the difference to the
365 preceding step is constrained.

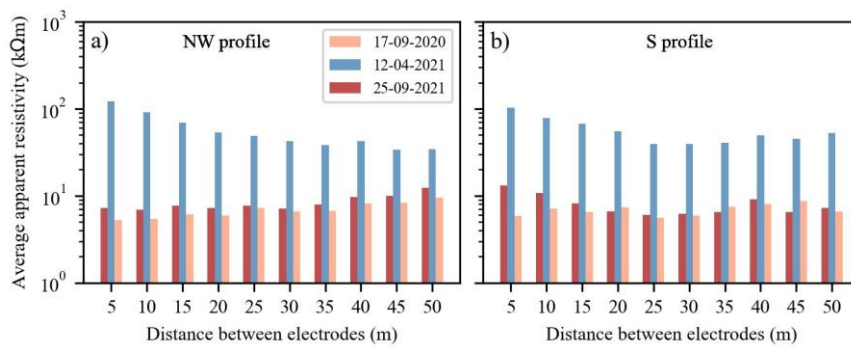
367 5. Results and interpretation

368 5.1. Overview of the raw data

369 Our interpretation of the ERT data starts with an analysis of the measured apparent
370 resistivity data, which can provide insights into subsurface conditions. Figure 5 shows the
371 variations in the average apparent resistivity associated with the same electrode distance or
372 pseudo-depth for three selected datasets from two profiles (NW and S profiles). The data reveal
373 the interannual and seasonal variations in the measured apparent resistivity, as well as the
374 differences between the two sides. During frozen conditions at the surface (dataset from 12-04-

375 2021), the apparent resistivity is almost the same on both sides (~100 to 120 kΩm near the
 376 surface), with only a slight decrease with depth at both sides. At the end of summer (dataset
 377 from 17-09-2021 and 25-09-2021), the resistivity values are higher in 2021 than in 2020 on
 378 both sides, which correlates with climatic data indicating that 2021 was a cooler year, on
 379 average (see Fig. 2). Secondly, on the NW~~north~~ face, the average resistivities increase with
 380 depth (from ~7 kΩ.m to ~12 kΩ.m), while on the south side, the average resistivities decrease
 381 with depth (approximately 13 kΩ.m at shallow depth to ~7 kΩ.m at greater depth). This
 382 difference in the trend between both sides could be interpreted by cooler conditions (permafrost
 383 at shallow depth) at north side and warmer conditions with thicker active layer at the south
 384 face. This difference in trend between the two sides can be attributed to cooler conditions on the
 385 north-face, where permafrost appears at shallow depth, and warmer conditions on the south-
 386 face, characterized by a drained and thicker thawed active layer. This observation is consistent
 387 with the temperature measurements from boreholes BH-NW and BH-S (see Fig. A1).

388



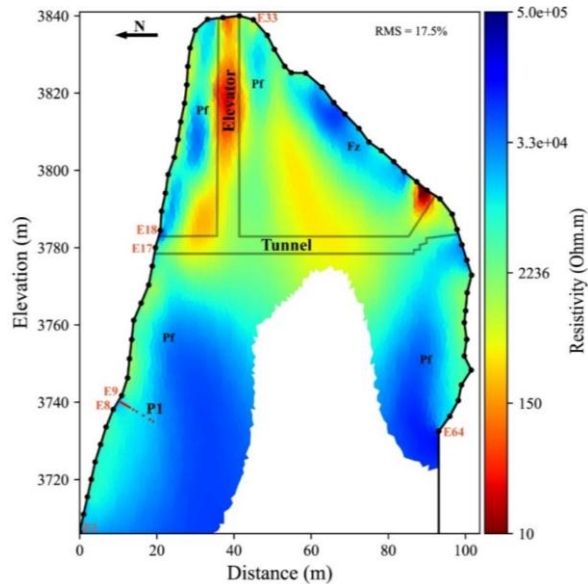
389

390 **Figure 5.** Seasonal variations of the average apparent resistivity at different distances between
 391 electrodes—distances within a quadrupole (*i.e.*, at varying depths of investigation). Data in spring
 392 showshows the same pattern on both sides. In autumn, there is a divergence in the trend of average
 393 resistivities with depth on both sides, that is related to the hydrothermal conditions at each side.

394

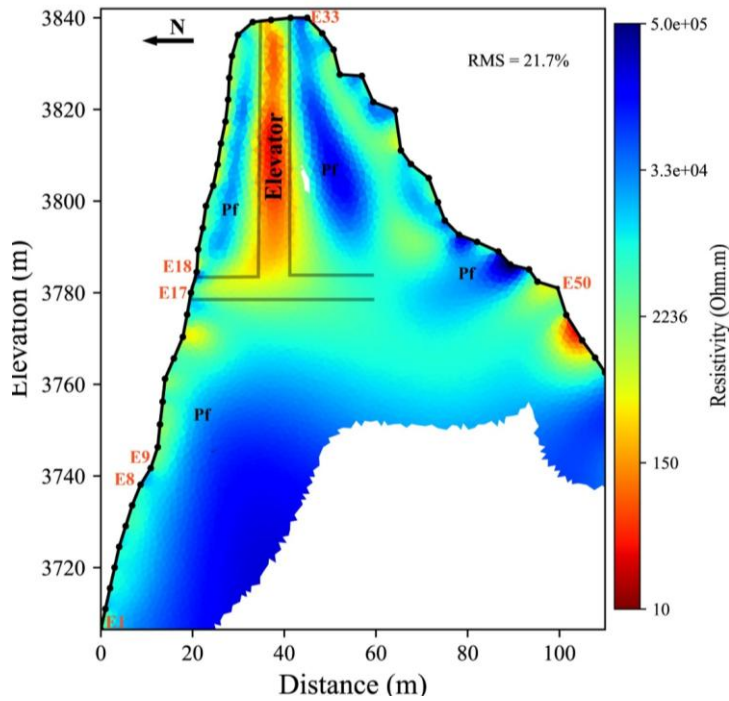
395 5.2. Internal structure of the site

396 In order to gain an overview of the internal structure of the study site based on the
397 resistivity distribution, we carried out inversions of two long profiles (NW+S and NW+E),
398 acquired with Wenner electrode arrays with 64 electrodes. Figure 6 shows the electrical
399 resistivity tomogram from late summer 2020 (August 26th, 2020), where acquisition on both
400 North-West and South sides (NW+S) was performed. The tomogram clearly reveals the site's
401 internal structure, with low resistivity areas (warm-colored zones) indicating the relative
402 positions of the infrastructure elements (elevator and galleries on both sides). It also shows the
403 extent of the active layer (moderate resistivity areas near the surface), as well as the permafrost
404 evidenced by high resistivity areas (represented in cool colors). Although the lower part of the
405 tomogram appears similar on both the NW and S profiles, which is expected since they lie in
406 rockwalls that are alike regarding slope and aspect (where the lowest part of the S profile is
407 deployed on the NW face as well, see Fig 1c), significant differences are evident in the upper
408 part (*i.e.*, above the gallery level), revealing the contrast between the sun-exposed (S side of
409 fractured granite and exposed to strong insolation) and shaded face (NW side of massive granite
410 mostly dependent on the sensible atmospheric heat flux). The upper part of the profile therefore
411 reveals strong thermal gradient typical of high-alpine summits (Noetzli et al., 2007; Magnin et
412 al., 2017). The high-resistivity area thus appears limited, likely due to the heat flux from the
413 sun-exposed and warm face towards the close shaded-face.
414



415
 416 **Figure 6.** Electrical resistivity tomogram over the NW+S profile measured on August 26, 2020. A total
 417 of 320 data points used for the inversion (475 data points constitute the complete pseudo-section), about
 418 30% of dataset was filtered. Grey lines indicate the approximative positions of infrastructure (galleries
 419 and elevator). Pf stands for Permafrost zone and Fz for Fractured Zone. E1 to E64 are Electrode
 420 numbers. Red dots at P1 indicate ~~the~~ positions of the thermal sensors in BH-NW.

421
 422 Figure 7 provides an example of the resistivity tomogram for the combined NW and E profiles.
 423 This tomogram highlights the changes in resistivity associated with permafrost, active layer,
 424 and anthropogenic installation (such as the elevator and gallery (relatively far from the profile
 425 at the E side compared to S profile)). On the eastern side, a thick and desiccated active layer (>
 426 5 m depth) is observed, with some resistive zones near the surface. Indeed, ~~¶~~ these resistive
 427 zones are likely fractured zones creating an unsaturated and air-filled zone and surrounded by
 428 moderate resistivity regions where fractures are filled closed or where water drainage is weak
 429 or absent.



430

431 **Figure 7.** Electrical resistivity tomogram over the profile NW+E at the end of summer (September 25
 432 [th, 2021](#)). [A total of 310 data points were used for the inversion \(475 data points constitute the complete](#)
 433 [pseudo-section\), about 35% of dataset was filtered](#). Data acquisition on the East profile runs
 434 into problems related to electrodes contact and cable malfunction. The last 10 electrodes from the E profile
 435 were removed during processing due to connection issues. Pf ~~and Fz~~ stands for Permafrost zone ~~and~~
 436 ~~Fractured Zone, respectively~~.

437

438 5.3. Seasonal and interannual variations

439 In order to track the seasonal and interannual variations in the permafrost, a time-lapse
 440 inversion approach was employed to invert datasets for each profile (NW, S). ~~The reference~~
 441 ~~model was moved along with the inversion so that the difference to the preceding step is~~
 442 ~~constrained~~. Figure 8 shows the tomograms of resistivity distribution after a time-lapse
 443 inversion of datasets ~~acquired along the from~~ NW profile at different time intervals. Spatial and
 444 temporal changes in resistivity ~~can~~ be observed, while the anomaly related to the gallery

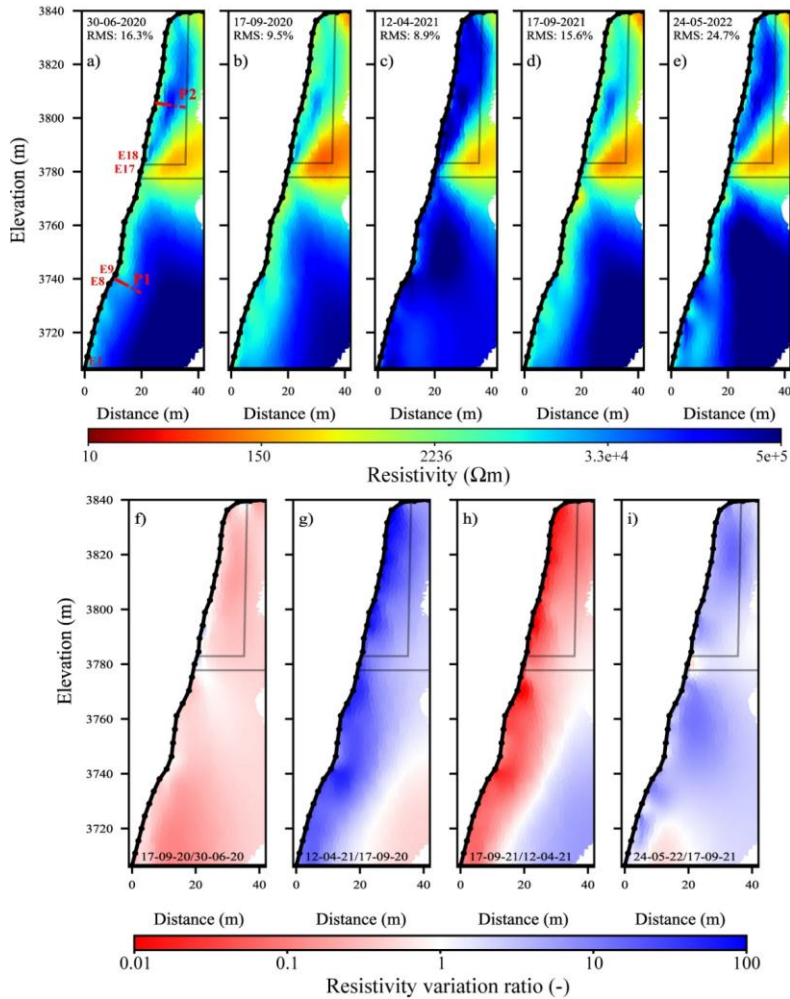
445 (the warm-colored area (low resistivity area)) remains consistent over time. The permafrost
446 ~~layer associated with identified by~~ high resistivity, is observed in two zones, above and below
447 the gallery. ~~According to temperature analyses conducted by Magnin et al. (2024),~~ 2021 was,
448 ~~on average,~~ cooler than both 2020 and 2022 ~~in coherence with air temperature (see Fig. 2), and~~
449 ~~this is.~~ This is reflected in the tomograms by a more prominent cool-colored zone (indicating
450 colder conditions) in 2021 compared to data in 2020 (Fig. 8b and d). Additionally, there is a
451 significant variation in the lower part of the tomograms in 2022 (Fig. 8e), which may be related
452 to water infiltration in fractures that shortcut the heat transfer from the surface to depth (Hasler
453 et al., 2011). However, this area is uncertain, as it is located at the border of the tomogram
454 where sensitivity is low. In addition, the RMS error is high in this tomogram, indicating high
455 uncertainties. Therefore, this information should be carefully considered and verified with
456 further measurements focused on the zone of interest. Unlike Offer et al. (2025), no evidence
457 of water ~~pressurization accumulation~~ was observed from the geophysical measurements on the
458 NW face. ~~This is most likely due to the distance between the monitored area and~~ It is suggested
459 ~~that~~ the water table ~~laying at about 1000 m lower~~ ~~lies at lower altitude~~ (Magnin and Josnin,
460 2021), ~~and that leads to water drainage.~~

461 Instead of analyzing temporal resistivity changes in absolute terms, Figure 8 (f - i)
462 illustrates the resistivity variation ratio between two subsequent measurements. This approach
463 facilitates the tracking and visualization of small changes in resistivity. A value of 1
464 (represented in white color) corresponds to no change in resistivity between the two
465 measurements (reflecting consistent geological conditions, topographic effects, infrastructure
466 or no considerable change in temperature over time), while the blue color indicates that the
467 resistivity increased over time, and the red color represents the inverse. It can be observed that
468 seasonal variations are the most pronounced, as illustrated in Figure 8g, h and i, compared to
469 short-term fluctuations (see Fig. D2). The effects of freezing and thawing are marked by

470 maximum variations near the surface (in the active layer). In contrast, over a short time interval
471 (*i.e.*, a few weeks), only minor variations are noted (*e.g.*, Fig. 8f, Fig. D2 b, e and j). The
472 decrease in resistivity near the surface at approximately 3780 m, observed in Figure 8i, could
473 be related to water flow around the gallery, where water circulation and percolation in the
474 galleries infiltration occurs every summer, ~~as noticed by local staff (personal~~
475 ~~communication~~ (Ben-Asher et al., 2025). Consequently, a specific water diversion system has
476 been installed to protect tourists from these water flows. Furthermore, at approximately 3740
477 m, close to borehole BH-NW, we observe variations in resistivity, with values higher than in
478 the surrounding zone, forming a vertical pattern visible in Figures 8b, d, and e. These features
479 coincide with open sub-vertical fractures that affect the temperature-depth profile in boreholes
480 (Magnin et al., 2015).

481 Extended times lapse inversion of datasets from NW and S face are presented in
482 appendix D.

483



484
 485 **Figure 8.** Seasonal and interannual variations of electrical resistivity at NW side. a - e) electrical
 486 resistivity tomograms at different dates (from June-2020 to June-2022). The conductive zone (in warm
 487 colors) denotes the presence of the gallery and elevator (see Fig. 6). The red dots (P1 in panel a) indicate
 488 the positions of the thermal sensors in the borehole BH-NW. Data presented on Figures 9, 10 and 11 are
 489 extracted at the red dots (P1 and P2). f - i) resistivity variation ratio between consecutive electrical
 490 resistivity tomograms. Blue colors indicate an increase in resistivity, while red colors represent a
 491 decrease in resistivity from one measurement to the next.

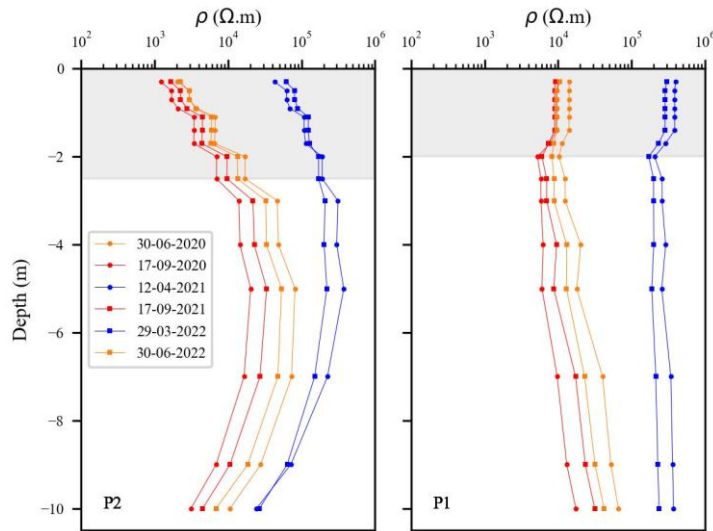
492

493

494

495 Inverted resistivities ~~values were extracted along profiles at~~ P1 (BH-NW) and P2,
 496 ~~corresponding to borehole BH-NW and a virtual borehole, respectively (see positions of P and~~
 497 ~~P2 in Fig. 8a), at P2 are presented in Figure 9.~~ The extracted resistivities (Fig. 9) show that the
 498 variation of resistivity with depth is more pronounced at P2 ~~than at P1~~. This greater variation
 499 could be due to a higher water content in the active layer or a thicker active layer at P2 compared
 500 to P1. The greater thickness of the active layer in the upper section can be explained by the 3D
 501 heat transfer and the proximity of the shaded face (NW side) to the sun-exposed faces (S side)
 502 in the top part (Magnin et al., 2017), ~~as well as the greater amount of direct sun-beams at the~~
 503 ~~summit than in the more shaded lower parts of the face. The 3D effects are well visible at depth~~
 504 ~~of P2, where resistivity decreases due to warmer conditions close to the opposite sun-exposed~~
 505 ~~face. Additionally, the presence of the elevator contributes to heating and cooling the granite~~
 506 ~~from inside.~~ In the lower section ~~at P1 (profile P1)~~, the contrast between the resistivity in the
 507 active layer and that in the permafrost is not significant. ~~This may be attributed to (i) snow~~
 508 ~~accumulation in this zone (see Fig. 1c), where the snowpack acts as a thermal insulator,~~
 509 ~~reducing temperature variability and leading to lower water content in the active layer; (ii) the~~
 510 ~~presence of fractures (as noted above) influencing the temperature-depth profile (see Fig. 8b, e~~
 511 ~~and d), possibly due to low water content (porosity is around 1%), or high surface conductivity~~
 512 ~~in granite.~~ However, it is important to note that the ALT is about 2.7 m at the end of summer
 513 ~~(from based on BH-NW measurements; see Fig. A1), whereas, and~~ the smallest quadrupole
 514 spacing is 15 m, ~~leading to effective depth around 2.55 m (Edwards, 1977),~~ which is insufficient
 515 to capture ~~the whole thin~~ variations close to surface ~~(Edwards, 1977)~~. Additionally, ~~there is a~~
 516 slight decrease ~~in of permafrost resistivity is observed over time in the permafrost from June~~
 517 ~~between 30 June 2020 to and 30 June 30, 2022. That is coherent with the observed permafrost~~
 518 ~~warming at 10 m depth (Magnin et al., 2024).~~ Finally, in 2021, resistivity values were higher in
 519 both the upper and lower parts ~~(at P1 and P2)~~ compared ~~with to~~ 2020 and 2022, ~~consistent a~~

520 trend that aligns with the temperature measurements (see Fig. 2, or details in Magnin et al.
 521 (2024)).



522
 523 **Figure 9.** Resistivity extracted over depths at different dates and locations (P1, P2). Resistivities
 524 extracted from tomograms in Fig. D1. There is greater variation at the higher profile (P2), where heat
 525 transfer from the nearby sun-exposed faces is more significant in the site's upper part.
 526

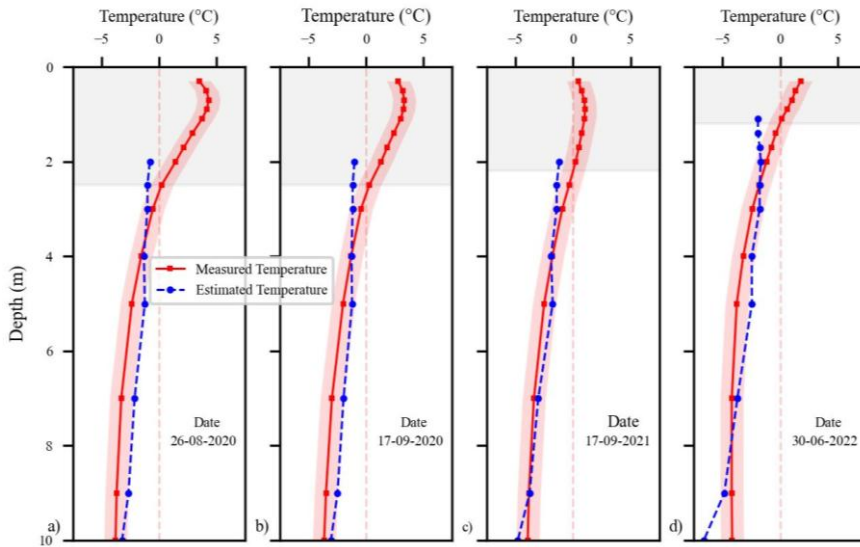
527 5.4. Temperature - resistivity relationship

528 Extracted resistivities at P1 are superimposed on borehole BH-NW, where temperature
 529 measurements are available. We are using these two datasets (*i.e.*, temperature and resistivity
 530 measurements at the same location, BH-NW) to explore the potential for estimating temperature
 531 based on electrical resistivity measurements and to perform a quantitative evaluation of the
 532 Temperature - Resistivity relationship determined in a laboratory.

533 It is known that, when temperature > 0 °C (*i.e.*, the case in the active layer), resistivity
 534 depends on multiple variables, including porosity, water content, water salinity, Cation
 535 Exchange Capacity (CEC) and temperature (Revil et al., 2018), which makes it difficult to
 536 model or predict the resistivity value in the active layer. In contrast, under frozen conditions,

537 resistivity of a medium is primarily controlled by the remaining unfrozen pore water content,
538 and is assumed to be dependent on temperature, while the other parameters remain constant.
539 Therefore, the extracted resistivities in the frozen zone were converted to temperature using the
540 petrophysical model in Equation 2 (Duvillard et al., 2021; 2018; Coperey et al., 2019). Figure
541 10 shows the measured temperature alongside the estimated temperature from ERT data, plotted
542 against depth at different dates (in summer and autumn). A good agreement can be observed
543 between the measured and estimated temperature in frozen conditions, with differences of less
544 than ± 1 °C at depths between 4 and 10 m. This suggests that temperature distribution across the
545 site can be calculated using this model (e.g., Duvillard et al., 2021), assuming the medium is
546 homogenous and resistivity variations are solely attributed to temperature. Figure 11 illustrates
547 the temperature distribution along the profile NW estimated from electrical resistivity
548 measurements acquired at different dates between June 2020 and June 2022. The estimated
549 temperatures vary consistently with the analyses presented above, revealing two permafrost
550 zones above and below the gallery. As rock surface temperature was measured in the galleries
551 as well for other purposes, we can also highlight that the positive temperature reaching up to
552 4°C around the gallery is in very good agreement with these measurements (Ben-Asher et al.,
553 2025). It can be observed a coherent temperature gradient through depth and positive
554 temperatures around and in the infrastructure. It can also be observed that temperature decreases
555 with depth, reaching values lower than -5 °C in the zone where ERT sensitivity is low or absent.
556 Furthermore, dHowever, at AdM, this condition is not satisfied due to the infrastructure, which
557 creates a conductive zone within the medium (see Figs. 6, 7). Predicting temperature in the
558 active layer is not feasible since temperature is not the dominant factor affecting resistivity. The
559 data collected under frozen surface conditions at the surface (i.e., measured in winter and spring
560 with high contact resistance) show large resulted in large discrepancy between the estimated

561 and measured temperature and ~~therefore cannot~~ not be reliably used for temperature
 562 estimation. ~~A ERT measurements still a challenge in frozen condition at surface.~~
 563



564
 565 **Figure 10.** Comparison between measured temperatures in BH-NW and estimated temperatures derived
 566 from geophysical measurements (*i.e.*, extracted resistivity values at different dates) using the
 567 petrophysical model in Equation 2. The gray-shaded area indicates the extent of the active layer at the
 568 time of measurement. The red-shaded zones show the ± 1 °C range around the measured temperature.

569
 570

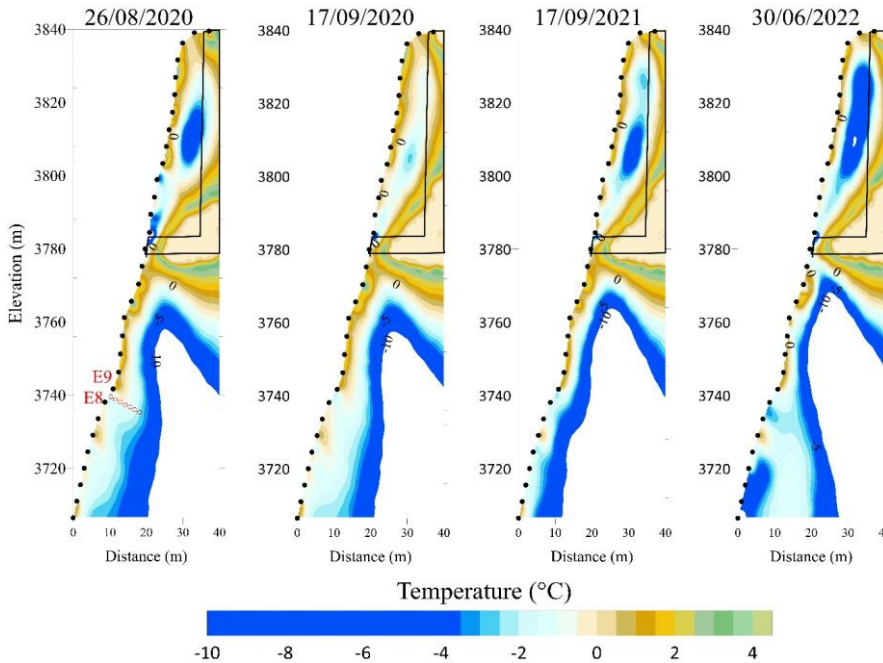


Figure 11. Spatio-temporal evolution of subsurface temperatures along the NW profile derived from electrical resistivity measurements, using Equation (2) and parameters obtained from laboratory measurements. Black dots indicate the electrode positions. The red circles indicate the location of borehole BH-NW, while the black lines mark the relative positions of the gallery and the elevator.

To go further in our analysis, Figure 12+ shows the extracted resistivity at P1 vs. temperature data measured in BH-NW at different dates. Laboratory measurements on two granite samples (labeled Sample AdM and Sample Cosmiques) are also shown. Three key observations can be made: i) Data collected in winter and spring (frozen conditions at surface), presented by blue symbols, show resistivity values higher than those expected from laboratory measurements, which aligns with the field observations reported by Maierhofer et al (2024). This may be related to the salt segregation during freezing, which may enhance conductivity of pore water and consequently reduce resistivity of samples. ii) At higher temperature (unfrozen conditions at surface), a linear trend is observed that aligns with laboratory measurements for

a mis en forme : Police :11 pt, Couleur de police : Noir, Police de script complexe :11 pt, (Complexe) Anglais (États-Unis)

a mis en forme : Police :Gras, Police de script complexe :Gras

a mis en forme : Police :11 pt, Couleur de police : Noir, Police de script complexe :11 pt, (Complexe) Anglais (États-Unis)

a mis en forme : Police :11 pt, Couleur de police : Noir, Police de script complexe :11 pt, (Complexe) Anglais (États-Unis)

a mis en forme : Retrait : Première ligne : 0 cm

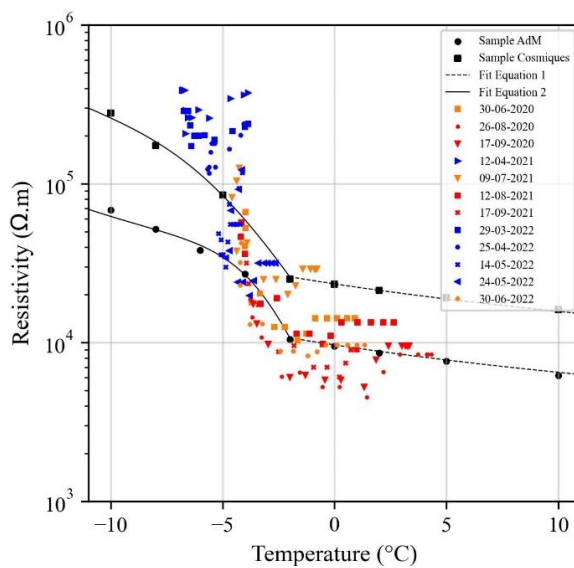
a mis en forme : Police :11 pt, Couleur de police : Noir, Police de script complexe :11 pt, (Complexe) Anglais (États-Unis)

a mis en forme : Police :11 pt, Couleur de police : Noir, Police de script complexe :11 pt, (Complexe) Anglais (États-Unis)

a mis en forme : Police :11 pt, Couleur de police : Noir, Police de script complexe :11 pt, (Complexe) Anglais (États-Unis)

a mis en forme : Police :11 pt, Couleur de police : Noir, Police de script complexe :11 pt, (Complexe) Anglais (États-Unis)

586 part of datasets (e.g., datasets of 26/08/2020 and 17/09/2020). The difference in resistivity
 587 between field and laboratory data under unfrozen conditions could be attributed to the
 588 heterogeneity at the field scale and/or the difference in water content and water salinity between
 589 laboratory and field environments. Whereas laboratory measurements were conducted in
 590 saturated conditions (saturation was performed under vacuum using degassed water). iii) Field
 591 data exhibit greater dispersion compared to laboratory data, which can be attributed to several
 592 factors, including 3D effects at the site, the influence of infrastructure and heterogeneity at
 593 different scales (from fractures scale to pore scale). In addition, there is a difference in
 594 resolution between the two field measurements: temperature measurements are local, while
 595 resistivity measurements account for a larger volume.



596
 597 **Figure 4412.** Resistivity vs. temperature. Resistivities are extracted from the tomograms in Figure D1
 598 at location P1. Temperature is measured by sensors at BH-NW. Laboratory data on two granite samples
 599 and fitting with Equation 1 and 2 are shown too.

600

601

602 5.5. Hydrogeological dynamics

603 One of the objectives of this study was to assess hydrogeological dynamics. Due to gaps
 604 in the ERT time series, the analysis of times series did not yield conclusive information.
 605 Therefore, we selected specific datasets (nearly complete pseudo-sections) and compared the
 606 results of the time-lapse inversion to gather information about water infiltration and drainage.
 607 Although we could not precisely identify the infiltration and drainage pathways or the water
 608 table (which may be located at a lower altitude according to Magnin and Josnin (2021)) using
 609 ERT measurements, we observed several instances that serve as evidence of possible water
 610 flows.

611 Figure 1342 shows the results of the time-lapse inversion of datasets along the S profile
 612 at various time intervals. The same inversion parameters were applied as those used to invert
 613 the datasets on the NW side (Fig. 8). In the upper part of the profile (i.e., above the gallery),
 614 seasonal variations in resistivity are influenced by the presence of fractures, which control affect
 615 the water flow pathways and consequently the resistivity response throughout signals
 616 during the seasonal cycle. This portion part of the profile is exposed to e characterized by strong
 617 insolation, which (i.e., sun exposed area) that dries the rock and fractures, leading to an
 618 increase in resistivity near the surface due to air-filled pores and fractures (e.g., Fig 12b-13a, c
 619 and le). Conversely, The decreases in resistivity in this zone (e.g., Fig 12a-13a, e, d and hg), can
 620 could be attributed to interpreted as a result of higher water saturation caused by the circulation
 621 of snowmelt or rainfall water. Snowmelt on this side supplies substantial amounts of water
 622 throughout the thawing season (Ben-Asher et al., 2023). The absence of precipitation data at
 623 the site prevented the correlation and validation of the ERT observations with rainfall events.
 624 Water infiltration and drainage in this area increase the ALT. The conductive zone observed
 625 beneath the desiccated fractured area (e.g., Fig. 13d and h) likely corresponds to zone results

a mis en forme : Police :Italique, Police de script complexe
:Italique

a mis en forme : Police :Italique, Police de script complexe
:Italique

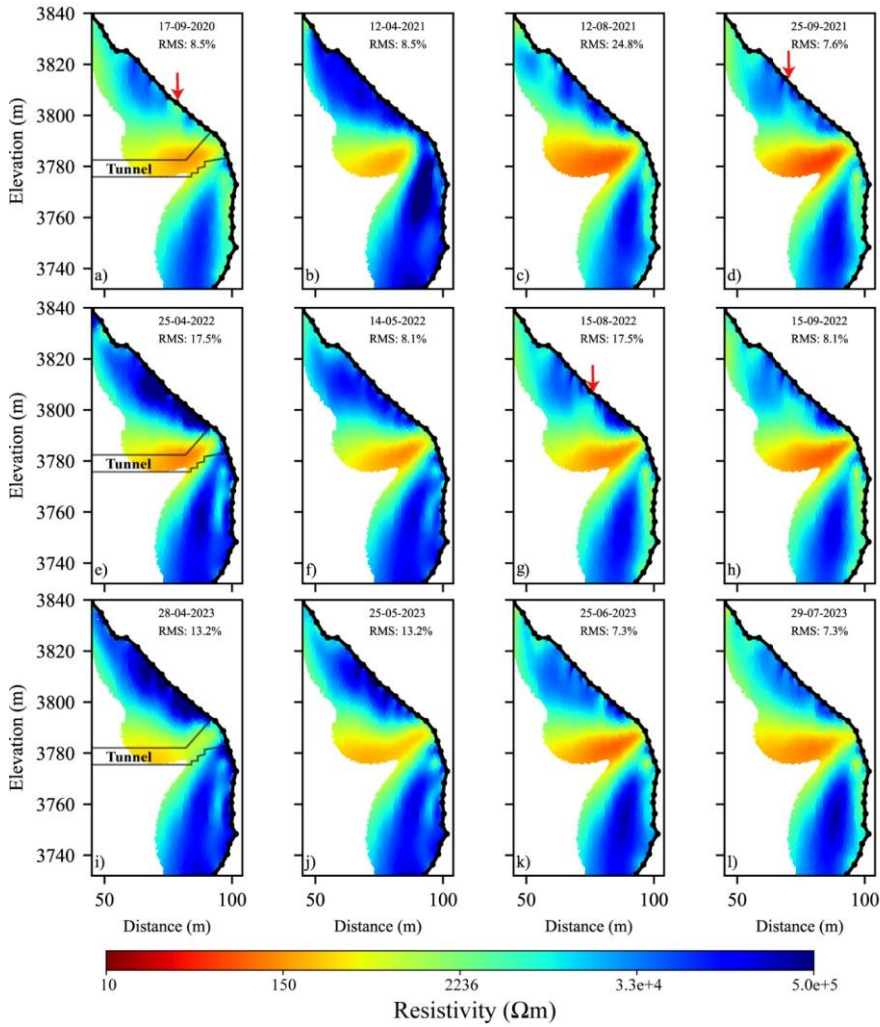
626 ~~from~~ of increased water saturation, as also reported by Sass (2004),~~minimal or nonexistent~~
627 ~~water drainage, which leads to higher water saturation.~~

628 In the lower part of the S profile (i.e., below the gallery), the seasonal variations in
629 permafrost resistivity are clearly observed and can be tracked over time, with no evidence of
630 significant water flow or drainage in this zone. This portion of the S profile shares a similar sun
631 exposure to the NW profile and therefore exhibits comparable dynamics, with the development
632 of a thawed and more water saturated active layer than in the upper part, because it is less
633 exposed to solar radiation, it undergoes less desiccation than the south face sector.

634

635

← a mis en forme : Gauche



636
 637 **Figure 12.13.** Tomograms of resistivity along the south side (S profile). Electrical resistivity tomograms
 638 at different dates (from September-2020 to July-2023). The conductive zone (in warm-colors) explained
 639 by the presence of the gallery. The red arrows indicate the potential zones of water infiltration from
 640 snowmelt or precipitation.

641
 642
 643
 644
 645

646

647 **6. Discussion**

648 In this study, we use repeated and automated ERT to investigate the evolution of
649 permafrost at a high ~~altitude mountain-rockwall~~ site. As expected, data from A-ERT are of
650 lower quality compared to manual measurements, where the operator can intervene to improve
651 CR after each electrode check (Doetsch et al., 2015; Hilbich et al., 2009). The high CR is the
652 main problem for getting good and durable A-ERT. Therefore, conducting ERT in frozen
653 surface conditions on rockwall permafrost remains challenging because of the high CR. Various
654 approaches were tested to improve CR. For instance, duplicated electrodes provided a durable
655 and significant improvement in CR (~ one order of magnitude reduction), helping to enhance
656 data quality.

657 Time lapse inversion of the measured resistivity showed the seasonal and interannual
658 variations (Fig. 8, ~~9~~ and ~~139~~). We observe that resistivity decreased over time at greater depths
659 (e.g., at P1 and P2, comparing data from July 30, ~~2020~~2020, and July 30, 2022), indicating
660 degradation of the permafrost such as also revealed by borehole measurements (Magnin et al.,
661 2024). However, this decrease in resistivity is minor, likely due to the relatively short
662 observation period of two years at NW side and ~~4~~four years at S side. A thicker active layer is
663 observed at the upper section, which can be attributed to 3D heat transfer processes and the
664 close proximity of the shaded north-west face to the sun-exposed southern faces in the upper
665 part of the slope (Magnin et al., 2017; Noetzli et al., 2007). ~~The presence of the galleries and
666 elevator contribute also to heating the granitic peak from inside decreasing the resistivity above
667 the tunnel.~~

668 The contrast between the resistivity in the active layer and that in permafrost is not
669 significant in the lower section on the NW side ~~at BH-NW~~ (P1 Fig. 9), which may ~~result from
670 be due to~~ low ice content/water content where the porosity is around 1 %, ~~the insulating effect
671 of snow accumulated in the zone of the BH-NW~~ or due to high surface conductivity in granite.

672 The alteration of granite involves the transformation of primary minerals (mica and alkali
673 feldspars) into secondary clay minerals (such as kaolinite), which are known for their high
674 cation exchange capacity and, consequently, their contribution to surface conductivity (Piolat
675 et al., 2025; Revil et al., 2024). Additionally, the sensitivity of the used electrode array
676 ~~dispositive~~ (with a smallest quadrupole length of 15 m) could affect the resolution of ERT
677 image near the surface (Binley and Kemna, 2005).

678 One of the objectives of this study was to evaluate the potential of using field resistivity
679 measurements to provide 2D or 3D information on thermal distribution in permafrost, based on
680 the superposition of resistivity and temperature datasets. The temperature estimation based on
681 ERT data leads to good agreement with observed temperatures, with differences of less than ± 1
682 $^{\circ}\text{C}$ at depths of 4 to 10m, indicating that the proposed model (Equation 2) can reasonably
683 reproduce subsurface permafrost temperatures. ~~indicate that the proposed model (Equation 2)~~
684 ~~can accurately reproduce temperatures in permafrost.~~ Consequently, this approach ~~could~~
685 provide valuable insights into the site's thermal distribution at the sites shown in Figure 11,
686 even though. ~~However, the internal temperatures of permafrost~~ temperatures typically lie ~~have~~
687 just a few degrees below freezing (e.g., Noetzli et al., 2024). A precision of ± 1 $^{\circ}\text{C}$ may be
688 insufficient in permafrost studies, where minor temperature variations can greatly impact
689 stability and long-term thermal evolution. Nevertheless, this level of accuracy remains within
690 the uncertainty range commonly reported for thermal models (Magnin et al., 2017).

691 On the other hand, predicting temperature in the active layer remains challenging, as
692 temperature is not the dominant factor affecting resistivity in thawed conditions. Data collected
693 under frozen surface conditions (i.e., measurements taken in winter and spring with high contact
694 resistance) resulted in larger discrepancy between estimated and measured temperature and
695 could not be reliably used for temperature estimation. Consequently A-ERT measurements
696 remain challenging when the ground surface is frozen, mainly due to the high contact resistance.

697 Furthermore, the transition between frozen and unfrozen conditions is not clearly
698 distinguished at resistivity curve extracted from field measurements (see Fig. 9, 10). The
699 freezing point, which is expected to result in a significant change in resistivity (as observed in
700 laboratory measurements), does not exhibit the same effect in field. However, some datasets
701 (e.g., datasets of 12/08/2021 and 17/09/2021) show progressive gradual increase in resistivity
702 when temperature decreased (*i.e.*, indicating progressive gradual freezing). This point needs to
703 be addressed in further research with smaller dispositive to a smaller electrode array to improve
704 the resolution of geophysical measurements.

705 On the sun exposed south face, the tomograms of resistivity show near-surface pore
706 desaturation, attributed to strong insolation on the rock face that is perpendicular to the sun
707 beam, along with features that may relate to water infiltration along fractures. The exact
708 pathways of infiltration and drainage are still ambiguous, possibly due to the resolution of
709 resistivity measurements. ~~Finally, w~~With the AdM setting, we can also hypothesize that the
710 saturated conditions are almost never reached. There is water circulation, but no pressurization
711 ~~accumulation~~ or development of a water column, because the water table is likely lower than
712 the area covered by the measurements (Magnin and Josnin, 2021), conversely to Offer et al.
713 (2025) at the Kitzsteinhorn for example. Indeed, our investigation is in a different setting: high
714 altitude peak lying ~2000-1000 m above the water table (Magnin and Josnin, 2021) while in the
715 Kitzsteinhorn outcrops from a glaciated areas with a probably much closer water table.

716 Finaly, A-ERT acquisition using smaller electrode array shorter spacing between
717 electrodes can improve the resolution near the surface resolution and could provide more
718 detailed information about the subsurface. Combining ERT with other geophysical methods,
719 such as induced polarization and/or refraction seismic tomography, can also provide
720 complementary petrophysical and spatial sensitivity, enabling a more comprehensive
721 investigation of the hydrogeological system of high mountain permafrost.

722

723 **7. Conclusions**

724 We used repeated and Automated Electrical Resistivity Tomography (A-ERT) to
 725 monitor permafrost dynamics over nearly four years at AdM in the French Alps, aiming to
 726 better understand the complexities of permafrost behavior in response to climatic variations and
 727 to explore the potential of the method for quantitative monitoring. The key findings are
 728 summarized as follows:

- 729 1. Through detailed analyses of ERT data, we were able to characterize the active layer
 730 dynamics and identify significant seasonal and multiannual changes in permafrost
 731 evolution~~dynamics~~. Importantly, we observed that the ALT and permafrost
 732 conditions below varied significantly from one face to another in coherence with
 733 climate signals and measured temperatures in boreholes. ~~The results underscore the~~
 734 ~~utility of ERT as a promising, non-invasive approach for monitoring permafrost~~
 735 ~~evolution in high mountains, enabling the identification of permafrost~~
- 736 2. This research demonstrates that temperature can be quantitatively accurately derived
 737 from geophysical measurements of electrical resistivity based on a petrophysical
 738 model connecting resistivity to temperature with precision of approximately ± 1 °C
 739 in frozen granite~~permafrost~~.
- 740 3. Our assessments of the hydrogeological system revealed instances of possible water
 741 flow as well as bedrock desiccation under strong insolation. ~~That said~~~~however~~, the
 742 exact pathways of infiltration and drainage remain unclear.
- 743 3.4. The results underscore the utility of ERT as a promising, non-invasive approach for
 744 quantitative monitoring non-linear permafrost evolution in high mountains.

745 Although installation of A-ERT system is relatively low costs, it requires substantial
 746 maintenance, especially on unstable high mountain rockwalls where rockfalls and lightning

747 effects lead to damaging of cable ~~problems~~. This study highlights the urgent need to address
748 challenges related to climate conditions at high-altitudes that affect device performance and
749 contact resistances, in order to enhance the reliability and durability of continuous A-ERT data
750 collection.

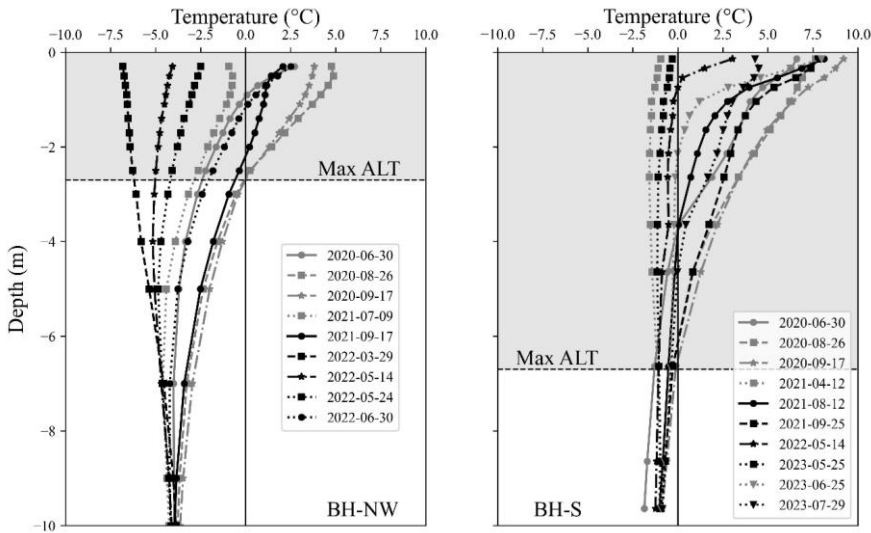
751
752 **Data availability.** Data will be made available on request to the corresponding author.

753 **Author contributions.** FA performed the data analysis, prepared the figures, and wrote the
754 majority of the text. JB contributed to data acquisition, writing, and figure preparation. FM and
755 AR contributed to the design of the ERT survey, as well as data acquisition and discussion of
756 the results. EM, MBA, LR and PAD contributed to the field installation and acquisition, JR
757 conducted and processed the laboratory data, MK contributed to data inversion and discussion,
758 TC provided air temperature data, ~~LR and PAD~~ offered additional information about the site.
759 Finally, all authors actively contributed to the preparation of this version of the paper.

760
761 **Competing interests.** The authors declare that they have no conflicts of interest.

762
763 **Acknowledgments.** This research is part of the ANR WISPER project (ANR-19-CE01-0018)
764 and the Action Plan on Risks from Glacial and Periglacial Origin (PAPROG) from the French
765 Ministry of Ecological Transition, Biodiversity, Forest, Sea and Fishing. The authors
766 acknowledge the following persons who ~~numerous people that~~ helped with the field work:
767 Antoine Chabas, Bruno Galabertier, Stéphane Jaillet and Raphaël Gallet from the EDYTEM
768 Laboratory, Simon Alesina from the University of Lausanne, Marc Cleriot for help ~~with field~~
769 ~~work~~, and Catherine Coulaud from IGE. The authors are also grateful for the Compagnie du
770 Mont-Blanc that provided access to the site and support.

771 **Appendix A: Temperature measurements in boreholes on different date BH-NW and**
 772 **BH-S**



773
 774 Figure A1: Temperature variation over depth in boreholes BH-NW and BH-S on different
 775 ~~date~~ dates aligned with the ERT measurement periods shown in Figures 8, 12 and D1. The gray-
 776 shaded area indicates the extent of the active layer at each borehole.

777

Appendix C: Summary of data presented in this study

a mis en forme : Centré

Table C1. Summary of data presented in this study. Number of data before filtering is 155 datum points of Wenner configuration. Most of datasets have more than 80% of total number of measurements. Two datasets have more than 40% of lost data because of disconnected electrodes.

Date	N-W Profile		S Profile	
	Number of data after filter	Percentage (%)	Number of data after filter	Percentage (%)
30-06-2020	151	97.5	-	-
26-08-2020	149	96.1	90	58
17-09-2020	151	97.5	90	58
12-04-2021	118	76.1	121	78
09-07-2021	114	73.5	-	-
12-08-2021	149	96.1	140	90.3
17-09-2021	145	93.5	131	84.5
25-09-2021	143	92.2	144	92.9
29-03-2022	121	78	-	-
25-04-2022	141	91	131	84.5
14-05-2022	141	91	147	94.8
24-05-2022	140	90.3	146	94.1
30-06-2022	102	65.8	-	-
30-07-2022	-	-	145	93.5
15-08-2022	-	-	145	93.5
15-09-2022	-	-	144	93
19-03-2023	-	-	138	89
28-04-2023	-	-	143	92.2
25-05-2023	-	-	148	95.5
25-06-2023	-	-	144	92.9
29-07-2023	-	-	140	90.3

Appendix D: Time lapse inversion results

a mis en forme : Centré

Appendix D presents time-lapse inversions of a large number of datasets from north-west face and south faces. The Resistivity variation ratio between consecutive electrical resistivity tomograms is also evaluated. A summary of these datasets is provided in Table 1C.

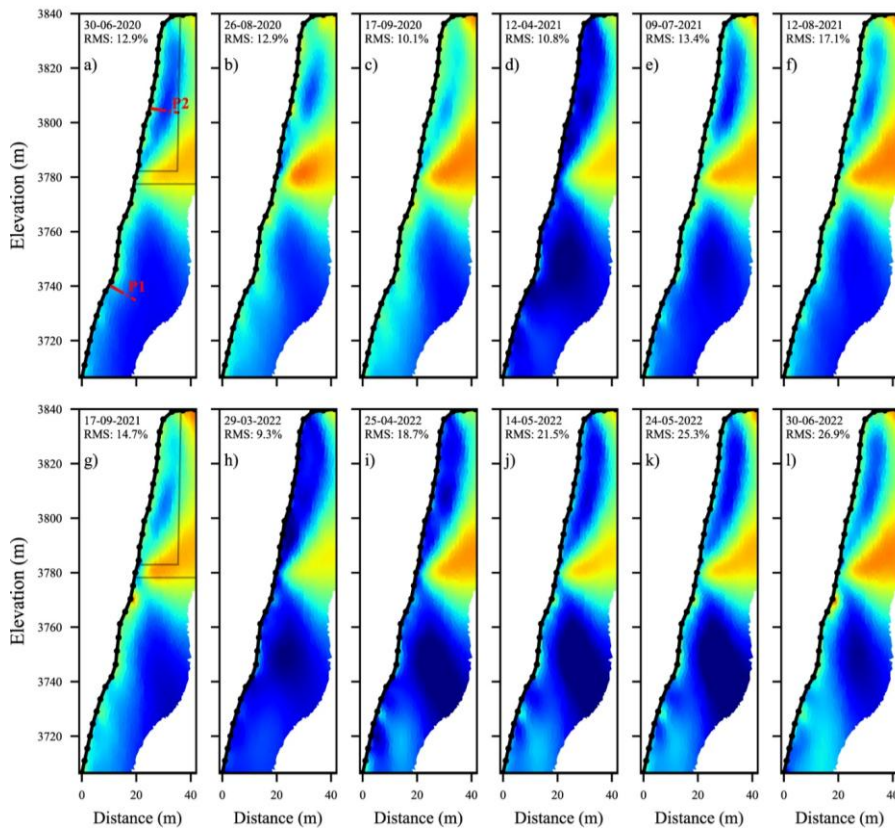
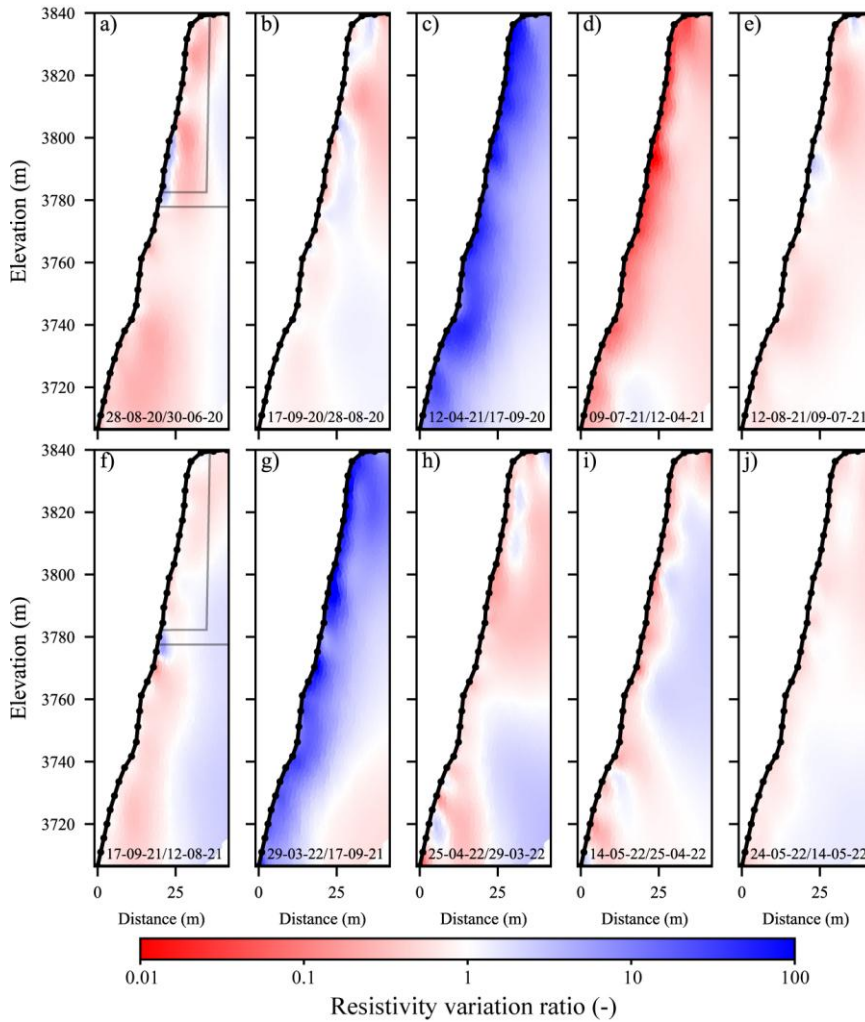


Figure D1. Electrical resistivity tomograms at different dates (from June-2020 to June-2022) along the NW side (NW profile). The conductive zone (in warm colors) indicates the approximate position presence of the gallery and elevator (see Fig. 6). The red dots (P1 in panel a) indicate the positions of the thermal sensors in the borehole BH-NW. Data presented on Figures 9, 10 and 11 are extracted at the the position of the red dots (P1 and P2).



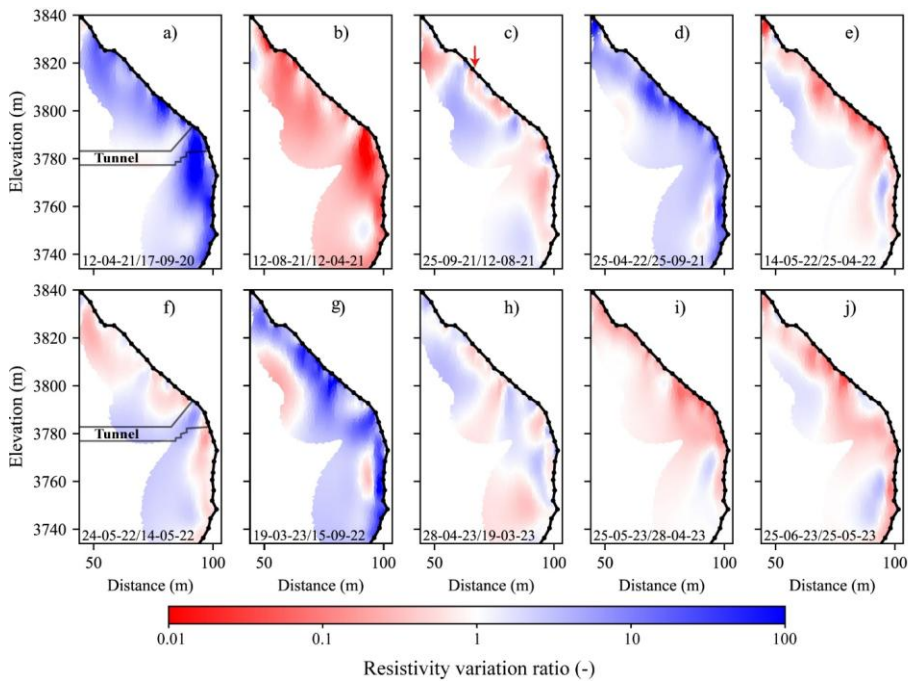
806

807 **Figure D2.** Resistivity variation ratio between consecutive electrical resistivity tomograms (shown in
 808 Fig. 9) along the NW side. Blue colors indicate an increase in resistivity, while red colors represent a
 809 decrease in resistivity from one measurement to the next.

810

811 Figure C3 illustrates the resistivity variation ratio between successive measurements on
 812 the S profile (Figure 12). The dynamics of the active layer are evident, with freezing-thawing
 813 effects visible near the surface (*e.g.*, Fig. D3a, d, and g). The heat effect (*i.e.*, decrease in

814 resistivity values near the surface) is more pronounced in the lower section (below the gallery).
 815 Another type of anomaly could be observed at greater depth, where heat and/or cool waves
 816 resulting of heat transfer (with delay) lead to local variations at greater depth (e.g., Fig. D3, e,
 817 g and i). In contrast, the fractured zone in the upper portion obscures the temperature
 818 dependency of resistivity due to fluctuations in air and water content (i.e., resistivity in this zone
 819 is impacted by factors beyond just temperature). Water infiltration in this area could explain the
 820 rapid and significant decrease in resistivity observed between 3790 and 3820 m a.s.l. (e.g., Fig.
 821 D3c, f, and j), which increases the thickness of active layer in this zone.



822
 823 Figure D3. Resistivity variation ratio between consecutive electrical resistivity tomograms (shown in
 824 Fig. 11) along the South side. Blue colors indicate an increase in resistivity, while red colors represent
 825 a decrease in resistivity from one measurement to the next. The red arrow shows the position of
 826 possible water infiltration inferred from the relative variation compared with the surrounding area.

827

References

- 828
- 829 Abdulsamad, F., Revil, A., Ghorbani, A., Toy, V., Kirilova, M., Coperey, A., Duvillard, P. A., Ménard,
830 G., and Ravel, L.: Complex conductivity of graphitic schists and sandstones. *Journal of*
831 *Geophysical Research: Solid Earth*, 124, 8223–8249. <https://doi.org/10.1029/2019JB017628>, 2019.
- 832 Ben-Asher, M., Magnin, F., Westermann, S., Bock, J., Malet, E., Berthet, J., Ravel, L., and Deline,
833 P.: Estimating surface water availability in high mountain rock slopes using a numerical energy
834 balance model, *Earth Surf. Dynam.*, 11, 899–915, <https://doi.org/10.5194/esurf-11-899-2023>,
835 2023.
- 836 [Ben-Asher, M., Chabas, A., Josnin, J.-Y., Bock, J., Malet, E., Poulain, A., Perrette, Y., and Magnin, F.:](#)
837 [Water flow timing, quantity, and sources in a fractured high mountain permafrost rock wall,](#)
838 [EGUsphere \[preprint\], <https://doi.org/10.5194/egusphere-2025-2450>, 2025.](#)
- 839 [Ben-Asher, M., Magnin, F., Westermann, S., Bock, J., Malet, E., Berthet, J., Ravel, L., and Deline,](#)
840 [P.: Estimating surface water availability in high mountain rock slopes using a numerical energy](#)
841 [balance model, *Earth Surf. Dyn.*, 11, 899–915, <https://doi.org/10.5194/esurf-11-899-2023>, 2023.](#)
- 842 Binley, A. and Kemna, A.: DC Resistivity and Induced Polarization Methods, in: *Hydrogeophysics,*
843 *Water Science and Technology Library book series*, edited by: Rubin, Y. and Hubbard, S.
844 S., volume 50, 129–156, https://doi.org/10.1007/1-4020-3102-5_5, 2005.
- 845 [Bruehl, R., Arthaud, F., Magnin, F., Napoleoni, R., Van Reeth, C., Augé, V., Sagot, C., Fructus, M.,](#)
846 [Birck, C., Choler, P., 2026. Different temperature responses of mountain rockwalls, soils, and lakes](#)
847 [to summer heat waves. *Reg Environ Change* 26, 34. <https://doi.org/10.1007/s10113-025-02517-3>](#)
- 848 Campbell, S., Rosa T. Affleck, Sinclair, S.: Ground-penetrating radar studies of permafrost, periglacial,
849 and near-surface geology at McMurdo Station, Antarctica. *Cold Regions Science and Technology*,
850 148, Pages 38–49, <https://doi.org/10.1016/j.coldregions.2017.12.008>, 2018.
- 851 Cathala, M., Bock, J., Abdulsamad, F., Deline, P., Josnin, J.-Y., Ravel, L., Revil, A., Richard, J.,
852 Verroust, F., and Magnin, F.: Assessing the role of permafrost in the preconditioning and triggering
853 factors of the September 2020 Crête des Grangettes rockfall (southern French Alps),

a mis en forme : Police :(Par défaut) +Titres CS (Times New Roman), Police de script complexe :+Titres CS (Times New Roman)

a mis en forme : Normal, Justifié, Retrait : Avant : 0 cm, Suspendu : 0.75 cm, Interligne : Double, Ne pas ajuster l'espace entre le texte latin et asiatique, Ne pas ajuster l'espace entre le texte et les nombres asiatiques

a mis en forme : Police :(Par défaut) +Titres CS (Times New Roman), Police de script complexe :+Titres CS (Times New Roman)

854 Géomorphologie: relief, processus, environnement, 30, 3, 171-188, <https://doi.org/10.4000/12yqn>,
855 2024.

856 [Cimpoiasu, M.O., Kuras, O., Harrison, H., Wilkinson, P. B., Meldrum, P., Chambers, J. E., Liljestrand,](#)
857 [D., Oroza, C., Schmidt, S. K., Sommers, P., Vimercati, L., Irons, T. P., Lyu, Z., Solon, A., and](#)
858 [Bradley, J. A. \(2025\). High-resolution 4D electrical resistivity tomography and below-ground point](#)
859 [sensor monitoring of High Arctic deglaciated sediments capture zero-curtain effects, freeze–thaw](#)
860 [transitions, and mid-winter thawing. The Cryosphere, 19, 401–421, \[https://doi.org/10.5194/tc-19-\]\(https://doi.org/10.5194/tc-19-401-2025\)](#)
861 [401-2025.](#)

862 Coperey, A., Revil, A., Abdulsamad, F., Stutz, B., Duvillard, P.A., and Ravel, L.: Low frequency
863 induced polarization of porous media undergoing freezing: preliminary observations and modeling,
864 Journal of Geophysical Research: Solid Earth, 124, doi:10.1029/2018JB017015, 2019.

865 Dahlin, T., and Zhou, B.: A numerical comparison of 2D resistivity imaging with 10 electrode arrays,
866 Geophys. Prospect., 52, 379–398. <https://doi.org/10.1111/j.1365-2478.2004.00423.x>, 2004.

867 Doetsch, J., Ingeman-Nielsen, T., Christiansen, A. V., Fiandaca, G., Auken, E., and Elberling, B.: Direct
868 current (DC) resistivity and induced polarization (IP) monitoring of active layer dynamics at high
869 temporal resolution, Cold Reg. Sci. Technol., 119, 16–28,
870 <https://doi.org/10.1016/j.coldregions.2015.07.002>, 2015.

871 Draebing, D.: Application of refraction seismics in alpine permafrost studies: A review, Earth-Science
872 Reviews, 155, 136–152, <https://doi.org/10.1016/j.earscirev.2016.02.006>, 2016.

873 Duvillard, P. A., Revil, A., Qi, Y., Soueid Ahmed, A., Coperey, A., and Ravel, L.: Three-Dimensional
874 Electrical Conductivity and Induced Polarization Tomography of a Rock Glacier, J. Geophys. Res.-
875 Sol. Ea., 123, 9528–9554, <https://doi.org/10.1029/2018JB015965>, 2018.

876 Duvillard, P.A., Magnin, F., Revil, A., Legay, A., Ravel, L., Abdulsamad, F., and Coperey, A.:
877 Temperature distribution in a permafrost-affected rock ridge from conductivity and induced
878 polarization tomography, Geophys. J. Int., 225, 1207–1221, <https://doi.org/10.1093/gji/ggaa597>,
879 2021.

a mis en forme : Police :(Par défaut) +Titres CS (Times New Roman), Police de script complexe :+Titres CS (Times New Roman)

- 880 Edwards, S. L.: A modified pseudosection for resistivity and IP. *Geophysics*, 42, 1020–
881 1036, <https://doi.org/10.1190/1.1440762>, 1977.
- 882 Etzelmüller, B., Czekirda, J., Magnin, F., Duvillard, P.-A., Ravel, L., Malet, E., Aspaas, A.,
883 Kristensen, L., Skrede, I., Majala, G. D., Jacobs, B., Leinauer, J., Hauck, C., Hilbich, C., Böhme,
884 M., Hermanns, R., Eriksen, H. Ø., Lauknes, T. R., Krautblatter, M., and Westermann, S.:
885 Permafrost in monitored unstable rock slopes in Norway – new insights from temperature and
886 surface velocity measurements, geophysical surveying, and ground temperature modelling, *Earth*
887 *Surf. Dynam.*, 10, 97–129, <https://doi.org/10.5194/esurf-10-97-2022>, 2022.
- 888 Farzaman M, Vieira G, Monteiro Santos FA, et al.: Detailed detection of active layer freeze-thaw
889 dynamics using quasi-continuous electrical resistivity tomography (Deception Island, Antarctica).
890 *Cryosphere*.14(3):1105-1120. <https://doi.org/10.5194/tc-14-1105-2020>, 2020.
- 891 Günther, T., Rücker, C., and Spitzer, K.: Three-dimensional modelling and inversion of dc resistivity
892 data incorporating topography-II. Inversion. *Geophysical Journal International*, Volume 166, Issue
893 2, August 2006, Pages 506–517, <https://doi.org/10.1111/j.1365-246X.2006.03011.x>, 2006.
- 894 Hartmeyer, I., Delleske, R., Keuschnig, M., Krautblatter, M., Lang, A., Schrott, L., and Otto, J.-C.:
895 Current glacier recession causes significant rockfall increase: the immediate paraglacial response
896 of deglaciating cirque walls, *Earth Surf. Dynam.*, 8, 729–751, [https://doi.org/10.5194/esurf-8-729-](https://doi.org/10.5194/esurf-8-729-2020)
897 2020, 2020.
- 898 Hasler, A., Gruber, S., Font, M., and Dubois, A.: Advective Heat Transport in Frozen Rock Clefts:
899 Conceptual Model, Laboratory Experiments and Numerical Simulation, *Permafrost and Periglacial*
900 *Processes*, 22, 378–389, <https://doi.org/10.1002/ppp.737>, 2011.
- 901 Hauck, C., Böttcher, M., and Maurer, H.: A new model for estimating subsurface ice content based on
902 combined electrical and seismic data sets, *The Cryosphere*, 5, 453–468, [https://doi.org/10.5194/tc-](https://doi.org/10.5194/tc-5-453-2011)
903 5-453-2011, 2011.
- 904 Hauck, C., and Hilbich C.: Preconditioning of mountain permafrost towards degradation detected by
905 electrical resistivity. *Environ. Res. Lett.* 19 064010. <https://doi.org/10.1088/1748-9326/ad3c55>,
906 2024.

- 907 Herring, T., Lewkowicz, A. G., Hauck, C., Hilbich, C., Mollaret, C., Oldenborger, G. A., Uhlemann, S.,
908 Farzamian, M., Calmels, F., and Scandroglio, R.: Best practices for using electrical resistivity
909 tomography to investigate permafrost, *Permafrost Periglac.*, 34, 494–512,
910 <https://doi.org/10.1002/ppp.2207>, 2023.
- 911 Hilbich, C., Marescot, L., Hauck, C., Loke, M. H., and Mäusbacher, R.: Applicability of Electrical
912 Resistivity Tomography Monitoring to Coarse Blocky and Ice-rich Permafrost Landforms,
913 *Permafrost Periglac.*, 20, 269–284, <https://doi.org/10.1002/ppp.652>, 2009.
- 914 Hilbich, C., Hauck, C., Hoelzle, M., Scherler, M., Schudel, L., Völksch, I., Vonder Mühll, D., and
915 Mäusbacher, R.: Monitoring Mountain permafrost evolution using electrical resistivity
916 tomography: A 7-year study of seasonal, annual, and long-term variations at Schilthorn, Swiss
917 Alps, *J. Geophys. Res.-Earth*, 113, F01S90, <https://doi.org/10.1029/2007JF000799>, 2008.
- 918 Jacquemart, M., Weber, S., Chiarle, M., Chmiel, M., Cicoira, A., Corona, C., Eckert, N., Gaume, J.,
919 Giacona, F., Hirschberg, J., Kaitna, R., Magnin, F., Mayer, S., Moos, C., van Herwijnen, A., and
920 Stoffel, M.: Detecting the impact of climate change on alpine mass movements in observational
921 records from the European Alps, *Earth-Science Reviews*, 258, 104886,
922 <https://doi.org/10.1016/j.earscirev.2024.104886>, 2024.
- 923 Karaoulis, M., Tsourlos, P., Kim, J., and Revil, A.: 4D time-lapse ERT inversion: introducing combined
924 time and space constraints, *Near Surf. Geophys.*, 12, 25–34, <https://doi.org/10.3997/1873-0604.2013004>, 2013.
- 926 Keuschnig, M., Krautblatter, M., Hartmeyer, I., Fuss, C. and Schrott, L.: Automated electrical resistivity
927 tomography testing for early warning in unstable permafrost rock walls around Alpine
928 infrastructure, *Permafrost Periglac.*, 28, 158–171. <https://doi.org/10.1002/ppp.1916>, 2017.
- 929 Krautblatter, M. and Hauck, C.: Electrical resistivity tomography monitoring of permafrost in solid rock
930 walls, *J. Geophys. Res.*, 112, F02S20, <https://doi.org/10.1029/2006JF000546>, 2007.
- 931 Krautblatter M., Verleysdonk S, Flores-Orozco A., and Kemna A.: Temperature-calibrated imaging of
932 seasonal changes in permafrost rock walls by quantitative electrical resistivity tomography
933 (Zugspitze, German/Austrian Alps). *J. Geophys. Res.*, 115, F02003,
934 <https://doi.org/10.1029/2008JF001209>, 2010.

- 935 Krautblatter, M., Funk, D. and G^unzl, F.K.: Why permafrost rocks become unstable: a rock–ice-
936 mechanical model in time and space. *Earth Surf. Process. Landforms*, 38, 876–887.
937 <https://doi.org/10.1002/esp.3374>, 2013.
- 938 Loke, M. H.: Time-lapse resistivity imaging inversion, paper presented at 5th Meeting of the
939 Environmental and Engineering Society European Section, Budapest. 1999.
- 940 Magnin, F., Deline, P., Ravanel, L., Noetzli, J., and Pogliotti, P.: Thermal characteristics of permafrost
941 in the steep alpine rock walls of the Aiguille du Midi (Mont Blanc Massif, 3842 m a.s.l), *The*
942 *Cryosphere*, 9, 109–121, <https://doi.org/10.5194/tc-9-109-2015>, 2015b.
- 943 Magnin, F., Krautblatter, M., Deline, P., Ravanel, L., Malet, E. and Bevington, A.: Determination of
944 warm, sensitive permafrost areas in near-vertical rockwalls and evaluation of distributed models by
945 electrical resistivity tomography, *J. geophys. Res.-Earth*, 120, 745–762,
946 <https://doi.org/10.1002/2014JF003351>, 2015a.
- 947 Magnin, F., Ravanel, L., Bodin, X., Deline, P., Malet, E., Krysiacki, J.-M., et al.: Main results of
948 permafrost monitoring in the French Alps through the PermaFrance network over the period 2010–
949 2022. *Permafrost and Periglacial Processes*, 35(1), 3–23. <https://doi.org/10.1002/ppp.2209>, 2024
- 950 Magnin, F. and Josnin, J.-Y. Water flows in Rock Wall permafrost: a numerical approach coupling
951 hydrological and thermal processes. *Journal of Geophysical Research - Earth Surface*, 126(11),
952 e2021JF006394. <https://doi.org/10.1029/2021JF006394>, 2021.
- 953 Magnin, F., Josnin, J.-Y., Ravanel, L., Pergaud, J., Pohl, B., and Deline, P.: Modelling rock wall
954 permafrost degradation in the Mont Blanc massif from the LIA to the end of the 21st century, *The*
955 *Cryosphere*, 11, 1813–1834, <https://doi.org/10.5194/tc-11-1813-2017>, 2017.
- 956 Maierhofer, T., Flores Orozco, A., Roser, N., Limbrock, J. K., Hilbich, C., Moser, C., Kemna, A., Drigo,
957 E., Morra di Cella, U., and Hauck, C.: Spectral induced polarization imaging to monitor seasonal
958 and annual dynamics of frozen ground at a mountain permafrost site in the Italian Alps, *The*
959 *Cryosphere*, 18, 3383–3414, <https://doi.org/10.5194/tc-18-3383-2024>, 2024.
- 960 Mewes, B., Hilbich, C., Delaloye, R., and Hauck, C.: Resolution capacity of geophysical monitoring
961 regarding permafrost degradation induced by hydrological processes, *The Cryosphere*, 11, 2957–
962 2974, <https://doi.org/10.5194/tc-11-2957-2017>, 2017.

- 963 Mollaret, C., Wagner, F. M., Hilbich, C., Scapozza, C., and Hauck, C.: Petrophysical Joint Inversion
964 Applied to Alpine Permafrost Field Sites to Image Subsurface Ice, Water, Air, and Rock Contents,
965 *Front. Earth Sci.*, 8, 1–25, <https://doi.org/10.3389/feart.2020.00085>, 2020.
- 966 Mollaret, C., Hilbich, C., Pellet, C., Flores-Orozco, A., Delaloye, R., and Hauck, C.: Mountain
967 permafrost degradation documented through a network of permanent electrical resistivity
968 tomography sites, *The Cryosphere*, 13, 2557–2578, <https://doi.org/10.5194/tc-13-2557-2019>, 2019.
- 969 Noetzi J., Gruber S., Kohl T., Salzmann N., Haeberli W.: Three-dimensional distribution and evolution
970 of permafrost temperatures in idealized high-mountain topography. *Journal of Geophysical*
971 *Research: Earth Surface* 112, n/a–n/a. <https://doi.org/10.1029/2006JF000545>, 2007.
- 972 Noetzi, J., Isaksen, K., Barnett, J. et al.: Enhanced warming of European mountain permafrost in the
973 early 21st century. *Nat Commun* 15, 10508. <https://doi.org/10.1038/s41467-024-54831-9>, 2024
- 974 Moser, C., Morra di Cella, U., Hauck, C., and Flores Orozco, A.: Spectral induced polarization survey
975 for the estimation of hydrogeological parameters in an active rock glacier, *The Cryosphere*, 19,
976 143–171, <https://doi.org/10.5194/tc-19-143-2025>, 2025.
- 977 Offer, M., Weber, S., Krautblatter, M., Hartmeyer, I., and Keuschnig, M.: Pressurised water flow in
978 fractured permafrost rocks revealed by borehole temperature, electrical resistivity tomography, and
979 piezometric pressure, *The Cryosphere*, 19, 485–506, <https://doi.org/10.5194/tc-19-485-2025>, 2025.
- 980 Pavoni, M., Boaga, J., Wagner, F. M., Bast, A., Phillips, M.: Characterization of rock glaciers
981 environments combining structurally-coupled and petrophysically-coupled joint inversions of
982 electrical resistivity and seismic refraction datasets, *Journal of Applied Geophysics*, 215, 0926-
983 9851, <https://doi.org/10.1016/j.jappgeo.2023.105097>, 2023.
- 984 ~~Piolat, L., Revil, A., Richard, J., Ghorbani G., Cosme, P., Géraud, Y., Casotti, C., Vaudelet, P., Diraison,~~
985 ~~843 M., and Favier, A., 2025. Induced polarization of volcanic rocks. 8. The case of intrusive~~
986 ~~igneous 844 rocks. Submitted, *Geophysical Journal International*~~
- 987 [Piolat, L., Revil, A., Richard, J., Ghorbani G., Cosme, P., Géraud, Y., Casotti, C., Vaudelet, P., Diraison,](#)
988 [M., and Favier, A.: Induced polarization of volcanic rocks. 8. The case of intrusive igneous](#)
989 [rocks, *Geophysical Journal International*, Volume 241, Issue 2, Pages 1348](#)
990 [1372, <https://doi.org/10.1093/gji/ggaf102>, 2025.](#)

- 991 Ravanel, L., Magnin, F. and Deline, P.: Impacts of the 2003 and 2015 summer heatwaves on permafrost-
992 affected rock-walls in the Mont Blanc massif. *Science of the Total Environment*, 609, 132–143.
993 <https://doi.org/10.1016/j.scitotenv.2017.07.055>, 2017.
- 994 Revil, A., Cathles, L. M., Losh, S., & Nunn, J. A.: Electrical conductivity in shaly sands with
995 geophysical applications. *Journal of Geophysical Research*, 103(B10), 23,925–23,936.
996 <https://doi.org/10.1029/98JB02125>, 1998.
- 997 Revil, A., Ghorbani, A., Zhao, X., Mouyexaux, A., Barrère, L., Richard, J., Peyras, L., and Vaudelet, P.
998 Groundwater flow paths using combined self-potential, electrical resistivity, and induced
999 polarization signals, *Geophysical Journal International*, 239, 2, 798–
1000 820, <https://doi.org/10.1093/gji/ggae291>, 2024.
- 1001 Revil, A., Coperey, A., Mao, D., Abdulsamad, F., Ghorbani, A., Rossi, M., and Gasquet, D. Induced
1002 polarization response of porous media with metallic particles — Part 8: Influence of temperature
1003 and salinity: *Geophysics*, 83, no. 6, E435–E456, <https://doi.org/10.1190/geo2018-0089.1>, 2018.
- 1004 Rucker, C., Günther, T., and Wagner, F. M.: pyGIMLi: An open-source library for modelling and
1005 inversion in geophysics, *Computers & Geosciences*, 109, 106–123,
1006 <https://doi.org/10.1016/j.cageo.2017.07.011>, 2017.
- 1007 [Sass, O.: Rock Moisture Fluctuations During Freeze-thaw Cycles: Preliminary Results from Electrical](#)
1008 [Resistivity Measurements, *Polar Geogr.*, 28, 13–31, <https://doi.org/10.1080/789610157>, 2004.](#)
- 1009 Scandroglio, R., Draebing, D., Offer, M., Krautblatter, M.: 4D quantification of alpine permafrost
1010 degradation in steep rock walls using a laboratory-calibrated electrical resistivity tomography
1011 approach, *Near Surface Geophys.*, 19, 241-260, <https://doi.org/10.1002/nsg.12149>, 2021.
- 1012 Smith, S.L., O'Neill, H.B., Isaksen, K. et al. The changing thermal state of permafrost. *Nat Rev Earth*
1013 *Environ* 3, 10–23 (2022). <https://doi.org/10.1038/s43017-021-00240-1>
- 1014 Steiner, M., Wagner, F. M., and Flores Orozco, A.: Improved characterization of alpine permafrost
1015 through structurally constrained inversion of refraction seismic data, *The Cryosphere Discuss.*,
1016 <https://doi.org/10.5194/tc-2019-52>, 2019.
- 1017 Steiner, M., Wagner, F. M., Maierhofer, T., Schöner, W., and Flores Orozco, A. Improved estimation
1018 of ice and water contents in alpine permafrost through constrained petrophysical joint inversion:

- 1019 The Hoher Sonnblick case study," *GEOPHYSICS* 86: WB61-WB75.
1020 <https://doi.org/10.1190/geo2020-0592.1>, 2021.
- 1021 Wagner, F. M., Mollaret, C., Kemna, A., and Hauck, C.: Quantitative imaging of water, ice and air in
1022 permafrost systems through petrophysical joint inversion of seismic refraction and electrical
1023 resistivity data, *Geophys. J. Int.*, 219, 1866–1875, <https://doi.org/10.1093/gji/ggz402>, 2019.
- 1024 Zimmermann, E., Kemna, A., Berwix, J., Glaas, W., Münch, H. M., and Huisman, J. A. A high accuracy
1025 impedance spectrometer for measuring sediments with low polarizability. *Measurement Science
1026 and Technology*, 19(10), 105603. <https://doi.org/10.1088/0957-0233/19/10/105603>, 2008.